# A Molecular Dynamics study of interfaces: from pure liquids to biological membranes

Jean-Pierre Nicolas

# A Molecular Dynamics Study of Interfaces:

## From Pure Liquids to Biological Membranes.

Academisch Proefschrift

*ter verkrijging van de graad van doctor*
*aan de Universiteit van Amsterdam*
*op gezag van de Rector Magnificus*
*prof. mr. P.F. van der Heijden*
*ten overstaan van een door het college voor promoties ingestelde*
*commissie, in het openbaar te verdedigen in de Aula der Universiteit*
*op donderdag 4 december 2003, te 11.00 uur*

door

Jean-Pierre Nicolas
geboren te Marseille, Frankrijk

Promotiecommissie:

Promotor:
Prof. Dr. Ir. B. Smit

Overige leden:
Prof. Dr. D. Frenkel
Prof. Dr. K. Hellingwerf
Prof. Dr. J.P.J.M. van der Eerden
Prof. Dr. A. Fasolino
Dr. T. Benvegnu

Faculteit der Natuurwetenschappen, Wiskunde en Informatica

Paranimfen:
Nicolas-Raphaël de Souza
Gooitzen Zwanenburg

Cover: From a slide introducing a poster I have presented in Lunteren on January 20th, 2000 ...

The work described in this thesis was performed at the Chemical Engineering Department, Faculty of Science, University of Amsterdam, Nieuwe Achtergracht 166, 1018 WV Amsterdam.

I let you make your own choice, mine is in **bold:**

Vulnerant omnes, ultima necat.
(in relation with *Hora est*, which ends the thesis defense).

Quand l'immédiat dévore, l'esprit dérive...
(Edgar Morin)

**à Corinne, pour tout,**
**et à Marie-Louise, qui m'a initié à la recherche.**

Le disciple n'est pas au-dessus de son maître,
mais tout disciple bien formé sera comme son maître.
(Luc, 6 40)

Voyager, c'est passer à côté.

Hep stourm ne vezer ket trec'h.

A sperenza, primà chì nasce, ultima chì more.

# Contents


**1 Introduction** **1**

1.1 Scope of this thesis . . . . . 2

1.2 Molecular simulations . . . . . 3

**A Pure liquids** **7**

**2 Surface tension calculation for liquid-vapour systems** **9**

2.1 Introduction . . . . . 9

2.2 Models and simulation methodology . . . . . 10

2.2.1 Force fields . . . . . 10

2.2.2 Simulations . . . . . 11

2.3 Results and discussion . . . . . 12

2.3.1 Liquid densities . . . . . 12

2.3.2 Surface tension estimations . . . . . 15

2.4 Concluding remarks . . . . . 17

2.5 Appendix: Surface tension calculation . . . . . 18

**3 The interfacial broadening of a liquid-liquid interface** **21**

3.1 Introduction . . . . . 21

3.2 Method and theory . . . . . 22

3.2.1 Molecular dynamics . . . . . 22

3.2.2 Interfacial ordering and width . . . . . 23

3.3 Results . . . . . 26

3.3.1 Molecular ordering . . . . . 26

3.3.2 Interfacial tension . . . . . 29

3.3.3 Interfacial width . . . . . 30

3.4 Discussion . . . . . 31

**B Surfactant activity** **35**

**4 Surfactin: a "chimeric" peptide** **37**
4.1 Introduction . . . . . 37
4.2 Methodology . . . . . 38
4.2.1 Molecular dynamics . . . . . 38
4.2.2 Structure analysis . . . . . 39
4.3 Results and discussion . . . . . 42
4.3.1 Behaviour at the interface . . . . . 42
4.3.2 Molecular shape and orientation . . . . . 47
4.3.3 Interactions between a surfactin and its environment . 55
4.3.4 Interfacial properties . . . . . 56
4.4 Concluding remarks . . . . . 60

**C Biological membranes** **63**

**5 Tetraether lipid membranes.** **65**
5.1 Introduction . . . . . 65
5.2 Molecular dynamics . . . . . 67
5.3 Results and discussion . . . . . 68
5.3.1 Mass and electronic density profiles . . . . . 68
5.3.2 Molecular orientation . . . . . 70
5.3.3 Pressure profiles . . . . . 73
5.4 Concluding remarks . . . . . 75

**Bibliography** **77**

**Summary** **87**

**Samenvatting** **89**

**Publications** **91**

**Acknowledgements** **93**

# Chapter 1

# Introduction

## Preamble: Surfaces, interfaces and surfactants

Let me imagine your environment as you are reading this manuscript, made of paper and ink (a suspension of carbon particles, *surfactants* and water). The booklet is laying on a table (a *surface*) in front of you, which has likely been cleaned recently with an appropriate detergent (containing *surfactants*). You are sipping a glass of "karnemelk", a sort of butter*milk* (a suspension of fat droplets, *surfactant* proteins and water) and you breath in peacefully (but not yet put to sleep, I hope), your lungs periodically filled in and out with air due to the layer of native *surfactants* covering the air cells, which can be roughly defined as a volume delimited by a *membrane*.

Now, we need to define few terms: an *interface* indicates a boundary between any two immiscible phases; a *surface* denotes an interface where one phase is a gas; a *surfactant* (a surface-active agent) is a substance that, when present at low concentration in a system, has the property of adsorbing onto the surfaces or interfaces of the system. A *membrane* is an interfacial layer or a barrier between two fluids. In a biological case, it contains embedded structures, as proteins, which under specific circumstances allow communications between the two separated phases.

Indeed, the aim of this Preamble is not to give an exhaustive (and exhausting) list of the processes involving an interface. This brief description only enumerates few common cases located at an interface (or surface) where surfactants may play a role. A more complete overview can be found in each introduction of the following chapters, which can readily be related to industrial processes and/or biological activities of a particular interest.

## 1.1 Scope of this thesis

In recent years, advances in several experimental techniques have contributed to our knowledge and understanding of the unique properties of the interfacial region. These include principally x-ray reflectivity, diffuse surface x-ray scattering, grazing incidence x-ray diffraction and scattering, and the optical techniques of ellipsometry, surface quasi-elastic scattering, sum frequency, and second-harmonic generation.

In order to both access to a microscopic description of molecules at an interface and study the interactions occurring within an interfacial domain as a membrane, we chose molecular simulation techniques. The recent improvements of computer performance, algorithms, and force fields, allow us to both simulate large systems and define molecules up to the atomic scale. This last point is especially important when looking at the interactions between molecules as lipid-protein interactions or between amino-acid residues and their environment, in general, everywhere where hydrogen bonds are involved.

Although it is straightforward to build a model of an interface made of two immiscible simple liquids, a realistic extension to biologically relevant systems is rather difficult; the lack of informations about interactions between membranes and embedded compounds or proteins, combined with the little information available on spanning protein structures, being the major limits.

The aim of this work is to characterize the topology and properties of various interfaces. To extend the insight given by molecular dynamics on the interfacial domain, we have implemented and probed a method to compute the pressure profile and the surface/interfacial tension of planar interfaces (the method is briefly presented in the Appendix of chapter 2).

We report in this manuscript a series of studies of planar interfaces:

- part A, where we probe a method to compute the pressure profile and the surface tension of a surface (chapter 2) and we describe the interfacial domain between oil and water, and its broadening (chapter 3),
- part B investigates the structural variability and dynamics of a small lipopeptide surfactant at an oil-water interface (chapter 4),
- part C presents the first molecular dynamics analysis of biological membranes made of tetraether lipids. A distinctive feature of these lipids is that they form planar membranes (or large liposomes) which are NOT a bilayer (chapter 5).

## 1.2 Molecular simulations

Depending on which properties we are interested in, different simulation techniques can be used. Molecules can be modelled at a mesoscopic, coarse-grained, atomic, or electronic scale [1]. Since we are ultimately interested in the dynamics of complex biological systems where molecular interactions need to be defined until the atomic scale, we chose to perform our simulations using the molecular dynamics technique [2, 3], where molecules are represented at an atomic, or pseudo-atomic scale (when hydrogen atoms do not need to be explicitly defined). Indeed, a fine degree of representation of the molecules has a price in terms of CPU time (computer time, thus money), and consequently restricts the properties we have access to. Fortunately, since many years, this limiting factor is decreasing tremendously by the improvement of computer power and the development of new algorithms.

### Molecular dynamics

Molecular Dynamics applies the laws of classical mechanics to compute the motion of the particles in a molecular system. Newton's second law reads:

$$\mathbf{F}_i = m_i \mathbf{a}_i = m_i \frac{\mathrm{d}\mathbf{v}_i}{\mathrm{d}t} = m_i \frac{\mathrm{d}^2 \mathbf{x}_i}{\mathrm{d}t^2}, \tag{1.1}$$

where $\mathbf{F}_i$ denotes the force on particle $i$ (resulting from an interaction potential between particles), $m_i$ its mass, $\mathbf{a}_i$ its acceleration, $\mathbf{x}_i$ its position, $\mathbf{v}_i$ its velocity, and $t$ is the time. Except very few cases which can be solved analytically, one needs to use numerical techniques to solve the equations of motion, yielding at each time step the new position, force, and velocity of each particle of the system. One of the integration algorithms used to solve these equations of motion is called the Verlet Leap Frog algorithm. This algorithm evaluates the velocities at half-integer time steps:

$$\mathbf{v}_i(t + \Delta t/2) = \mathbf{v}_i(t - \Delta t/2) + \mathbf{a}_i \Delta t \tag{1.2}$$

The positions are then advanced using the new velocities:

$$\mathbf{x}_i(t + \Delta t) = \mathbf{x}_i(t) + \Delta t \mathbf{v}_i(t + \Delta t/2), \tag{1.3}$$

the velocity at time $t$ being obtained from the average of the velocities half a time step either side of time $t$:

$$\mathbf{v}_i(t) = 1/2(\mathbf{v}_i(t + \Delta t/2) + \mathbf{v}_i(t - \Delta t/2)) \tag{1.4}$$

At each time step, the temperature, potential and kinetic energies are computed. From the study of the trajectories, transport properties can be estimated.

Molecules are modeled from connected particles (atoms, or pseudo-atoms consisting of one heavy atom (carbon (C), nitrogen (N), phosphorus (P), or oxygen (O),...), and two or three hydrogen atoms (H)), which interact by intermolecular and intramolecular potentials. The potentials used in this work are typically of the form:

$$U^{vanderWaals}(r_{ij}) \approx U_{LJ}(r_{ij}) = 4\epsilon \left[ \left( \frac{\sigma}{r_{ij}} \right)^{12} - \left( \frac{\sigma}{r_{ij}} \right)^{6} \right], \tag{1.5}$$

$$U^{electrostatic}(r_{ij}) = \frac{1}{4\pi\epsilon_0} \frac{q_i q_j}{r_{ij}}, \tag{1.6}$$

$$U^{bond}(r_{ij}) = \frac{1}{2} k_{bond}(r_{ij} - r_o)^2, \tag{1.7}$$

$$U^{bend}(\theta_{jik}) = \frac{1}{2} k_{bend}(\theta_{jik} - \theta_0)^2, \tag{1.8}$$

$$U^{dihedral}(\phi_{ijkn}) = \frac{1}{2} k_{dihedral}(\phi_{ijkn} - \phi_0)^2, \tag{1.9}$$

where $r_{ij}$ denotes the distance between the particles $i$ and $j$, $\epsilon$ and $\sigma$ the Lennard-Jones parameters, $q_i$ the partial electrostatic charge on the particle $i$, $\epsilon_0$ the dielectric constant, $k$ the force constant, $r_o$, $\theta_0$, and $\phi_0$, the equilibrium values of the bond length, the bending angle, and the dihedral angle, respectively (see the figure below).

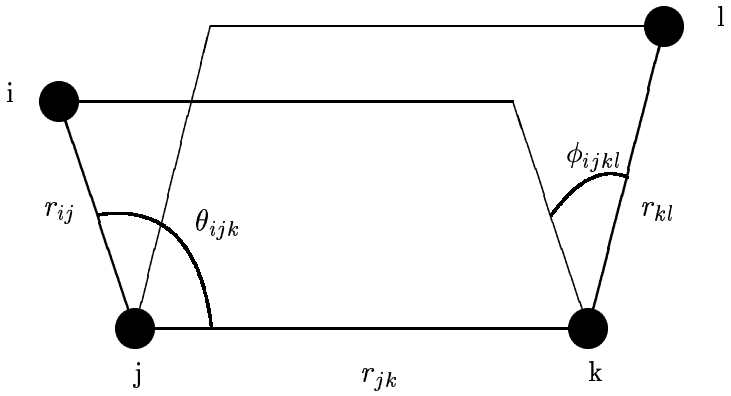

These equilibrium values, partial charges, intermolecular potential parameters, and force constants, define a set of parameters called a force field. Depending on the system and the properties we are looking at, each force field might give a slightly different representation of the system.

In this work, we have used the latest version of one of the two most efficient force fields existing for the modelling of biological molecule, the CHARMM force field, for the dynamics study of biological systems, as membranes or peptides. Alkanes have been represented by three different force fields, specific to this kind of molecules.

# Part A

# Pure liquids

# Chapter 2

# Surface tension calculation for liquid-vapour systems*

## 2.1 Introduction

Alkanes are an important class of molecules that occur in many practical applications. These last few years, many molecular models have been developed to describe the interactions between alkanes [4–9]. In these studies the models have been tested via a comparison with the experimental vapour-liquid coexistence curve. Subsequently, these models have been further validated via a comparison of the simulated and experimental diffusion coefficients [10] and viscosities [11, 12]. Less attention has been given to the surface tension.

In this chapter, we compare the predictions of two different alkane models to obtain some insight in the dependence of the computed surface tension on the details of the intermolecular interactions. We have computed the surface tension for the linear alkanes ($n$-hexane, $n$-decane and $n$-hexadecane) using OPLS [13] and SKS [4] (developed by Smit, Karaborni, and Siepmann) force field models. We have performed the simulations in two temperature ranges. One temperature range is the same as in ref. [14] in which Alejandre and co-workers have computed the surface tension of hexane at coexistence (vapour-liquid) for high temperatures using the SKS and de Pablo [15, 16] models. Our results for the surface tension of the hydrocarbons can be compared with the simulation data of Alejandre and co-workers. This allows us to validate our program and extend their results to other chain lengths and

*based on: J.P. Nicolas and B. Smit. Molecular dynamics simulations of the surface tension of $n$-hexane, $n$-decane and $n$-hexadecane. *Molecular Physics.* **100**, 2471–2475, 2002.

temperatures. To the best of our knowledge, there is no experimental data available for these systems at coexistence. Therefore, we do not know how accurately these alkane models can predict the surface tension. Experimental data are available at much lower temperatures, at densities higher than the coexistence density. We performed simulations at these conditions to assess the accuracy of the computed surface tensions.

In this chapter, we first describe the models used during our simulations, and then compare the densities and surface tension values predicted by our simulations with previous results and available experimental data. The method implemented for the surface tension calculation is described in the appendix 2.5.

## 2.2 Models and simulation methodology

### 2.2.1 Force fields

We calculate the surface tension for liquid/gas systems of the linear alkanes: hexane, decane, hexadecane. Two sets of force fields, SKS and OPLS, are compared.

We use the united-atom representation, which means that every methylene ($-CH_2-$) or methyl ($-CH_3$) group is modelled as a single interaction site. Three types of potentials are employed: nonbonded interaction, bond bending potentials, and torsion potentials. The nonbonded interactions between united atoms of different molecules and within a molecule (if two atoms are more than four atoms apart) are described with a Lennard-Jones potential. The interactions are truncated and shifted with a cut-off radius $r_c$:

$$U(r_{ij}) = \begin{cases} U(r_{ij})^{\mathrm{LJ}} - u(r_c)^{\mathrm{LJ}} & r_{ij} \leq r_c \\ 0 & r_{ij} > r_c \end{cases} \tag{2.1}$$

with

$$U(r_{ij})^{\mathrm{LJ}} = 4\epsilon_{ij}\left[\left(\frac{\sigma_{ij}}{r_{ij}}\right)^{12} - \left(\frac{\sigma_{ij}}{r_{ij}}\right)^{6}\right], \tag{2.2}$$

where $r_{ij}$ is the distance between united atoms $i$ and $j$, $r_c$ is the cut off distance, $\epsilon$ and $\sigma$ are Lennard-Jones energy and distance parameters, respectively. The numerical values of these parameters are shown in table 2.1. $\epsilon_{ij}$, $\epsilon_i$, $\epsilon_j$ and $\sigma_{ij}$, $\sigma_i$, $\sigma_j$ are related by $\epsilon_{ij} = \sqrt{\epsilon_i \epsilon_j}$ and $\sigma_{ij} = (\sigma_i + \sigma_j)/2$, respectively.

| | $-CH_2-$ | | $-CH_3$ | | |
|---|---|---|---|---|---|
| | $\sigma$ (Å) | $\epsilon$ (K) | $\sigma$ (Å) | $\epsilon$ (K) | $r_c$ (Å) |
| SKS | 3.93 | 47.0 | 3.93 | 114 | 13.8 |
| OPLS | 3.905 | 59.4 | 3.905 | 88.1 | 11.5 |

Table 2.1: *Values of Lennard-Jones parameters and $r_c$ from SKS and OPLS models [4, 17], respectively.*

We use the SHAKE algorithm [18] to impose a fixed bond length of 1.53 Åbetween two connected united atoms. The bond-bending potential [19] is given by:

$$U^{\text{bend.}}(\theta) = \frac{1}{2} k_\theta (\theta - \theta_0)^2 , \tag{2.3}$$

where $\theta$ is the angle between two connected bonds, and $\theta_0$ the equilibrium value of this angle, $k_\theta$ the force constant. We have used $k_\theta = 62500$ K.rad$^{-2}$ for both models, $\theta_0 = 112°$ in the OPLS model and 114° in the SKS model.

The torsion potential is defined for the OPLS model [17]:

$$U^{\text{tors.}}_{OPLS}(\phi) = \sum_{k=0}^{5} c_k \cos^k(\phi) , \tag{2.4}$$

and for the SKS model :

$$U^{\text{tors.}}_{SKS}(\phi) = 0,5 \left[ c_1 (1 + \cos\phi) + c_2 (1 - \cos 2\phi) + c_3 (1 + \cos 3\phi) \right] , \tag{2.5}$$

where $\phi$ is the dihedral angle. In the OPLS model, we use $c_0 = 1116$ K, $c_1 = 1462$ K, $c_2 = -1578$ K, $c_3 = -368$ K, $c_4 = 3156$ K, $c_5 = -3788$ K. For the SKS model we use $c_1 = 355$ K, $c_2 = -68.19$ K and $c_3 = 791.3$ K.

### 2.2.2 Simulations

Our simulations are performed in an NVT ensemble [20], i.e., with constant number of particles, volume and temperature. The equations of motion are solved using the Verlet Leapfrog integration algorithm [2]. The SHAKE method [18] is used to constrain the bond lengths. Simulations are run with periodic boundary conditions. We have used the DLPOLY program [21] for all our simulations.

At high temperatures, we have investigated the system at vapour-liquid coexistence (with liquid and gas densities obtained from Gibbs-ensemble simulations) and at low temperatures the system is defined "off coexistence"

(with experimental liquid densities and vacuum). At coexistence we compare our simulation results with those from Alejandre *et al.* [14] and at lower temperatures with experimental data [22, 23].

The simulations at coexistence are initiated in the following way. First, we construct a cubic box with molecules placed on a lattice at the estimated liquid density from Gibbs-ensemble computations [4]. For hexane, decane, and hexadecane the simulation cell contains 675, 405, and 300 molecules, respectively. This box is equilibrated during 50 000 time steps with a time step duration $\Delta t = 3fs$. This liquid box is "sandwiched" by two empty cubic simulation cells and these boxes are filled with a few alkane molecules to obtain the vapour coexistence density.

At low temperatures, off coexistence, we initiate the simulation at the liquid density taken from experimental data. At this temperature range, the vapour pressure is so low that the gas boxes contain on average less than one molecule. Therefore, we use for these simulations empty boxes and run a few hundreds steps in order to stabilize the interface. After this equilibration, liquid and gas boxes have approximately the same volume and the box length in $z$ direction exceeds 100 Å.

We accumulate surface tension values every 500 steps during 3 ns. These data are analysed using the block average method [24].

## 2.3 Results and discussion

### 2.3.1 Liquid densities

Before discussing the results for the surface tension, we compare the simulated liquid densities for the various models with experimental data. An example of a computed density profile of hexane at coexistence using the SKS model is presented in figure 2.1. This plot shows liquid-vapour coexistence. Because of the periodic boundary conditions we obtain two interfaces. From this figure we can compute the coexistence densities of the liquid with reasonable accuracy. Good agreement is found between results from simulations and those from experiments [25]. For the gas density, however, the number of molecules is too small to determine the coexistence gas density accurately. Figure 2.2 shows the coexistence liquid densities for hexane at various temperatures as obtained from our simulations using the SKS model. This figure shows that the Gibbs ensemble results [4] are in reasonable agreement, but not perfect, with the present simulations. Important to note is that the Gibbs ensemble simulations use a truncated potential [4] while in this work a truncated and shifted potential is used. For a simple Lennard-

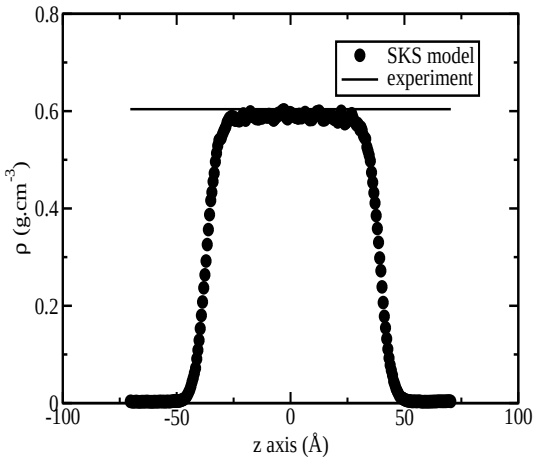


Figure 2.1: *Density profile ($\rho$) of* n*-hexane at coexistence at 350 K as obtained from the molecular dynamic simulations using the SKS model. The solid line gives the experimental value of alkane liquid density at 350 K [25].*

Jones fluid a truncated but not shifted potential has a 10% higher critical temperature (Tc) [26,27]. A similar shift of the critical temperature has been observed here. In figure 2.2, we also compare our results with the MD simulations of Alejandre *et al.* [14]. Alejandre *et al.* used a similar method as in the present work to compute the coexistence properties. However, in the work of Alejandre *et al.* a slightly larger cut off radius (15.8 Å) together with an inhomogeneous tail correction were used compared to Gibbs ensemble simulations [4, 28]. This results in a higher $T_c$ and hence a higher coexistence density compared to our simulations. For hexane also the OPLS model gives a good description of the experimental data. Concerning the highest temperature (450 K), the interfaces are too broad to yield an accurate estimation of the liquid density.

For $n$-decane and $n$-hexadecane figure 2.2 shows that the SKS model predicts a lower liquid density, compared to the OPLS model which is consistent with the conclusion in ref. [4] that the OPLS model overestimates the critical temperatures for long-chain alkanes.

In figure 2.3, we compare the simulated liquid densities at low temperature (off coexistence), using the SKS model, with the experimental liquid densities. For $n$-decane and $n$-hexadecane the agreement with the experimental data is very good, while for $n$-hexane, the simulations underestimate the liquid densities.

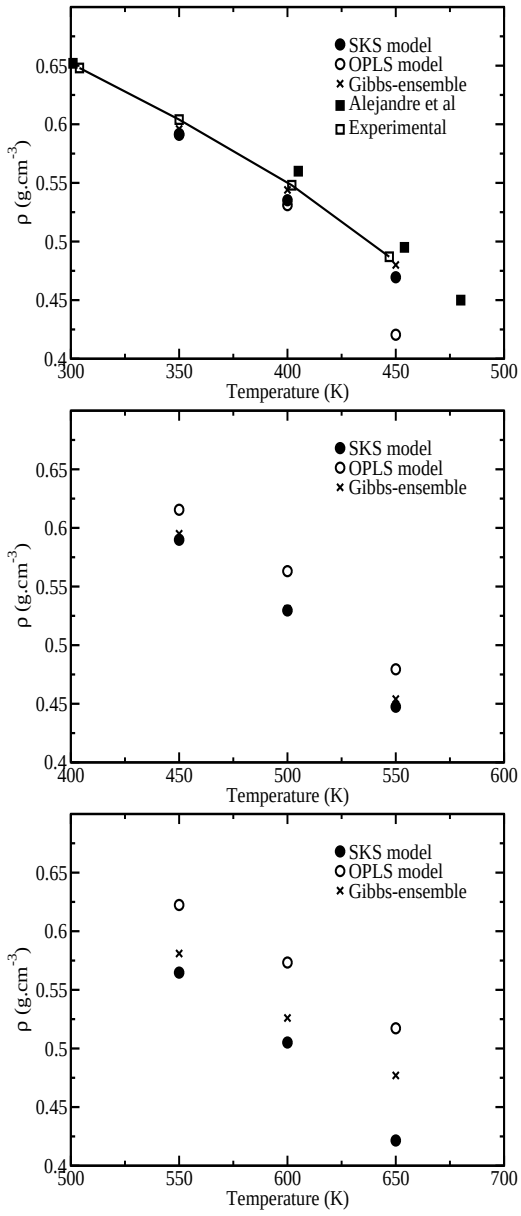


Figure 2.2: *Comparison of the liquid coexistence densities ($\rho$), for* n*-hexane (top),* n*-decane (centre), and* n*-hexadecane (bottom), as a function of temperature for the present work, the Gibbs ensemble results [4], the results from previous molecular dynamic simulations [14] and experimental results concerning* n*-hexane [25].*

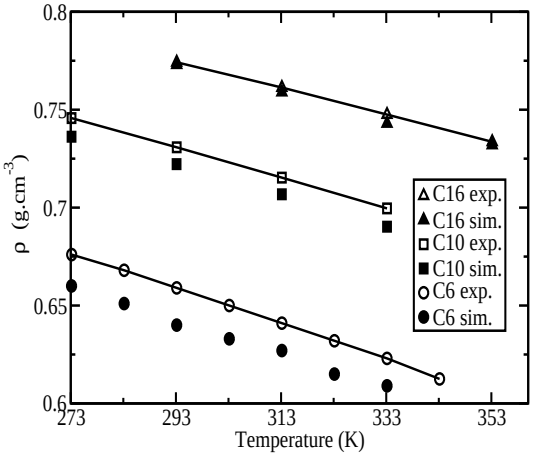


Figure 2.3: *Density $\rho$ as a function of the temperature for* n-*hexane (C*6*),* n-*decane (C*10*), and* n-*hexadecane (C*16*) from our simulations (SKS model) and from experiments.*

### 2.3.2 Surface tension estimations

In figure 2.4, the computed surface tension for hexane, decane, and hexadecane at coexistence are shown as a function of the temperature and density. To the best of our knowledge experimental data for these systems have not been published. For hexane we can compare the surface tension as a function of temperature as obtained by our simulations with previous results [14]. The agreement between these two studies is satisfactory; the small differences can be related to the larger cut-off radius used by Alejandre *et al.* For the OPLS model a similar result is obtained. If we plot the results versus liquid densities the differences between the various models become much smaller.

For decane and hexadecane the differences between simulated surface tension as a function of the temperature of the OPLS and SKS model are larger compared to hexane. Also for these molecules the differences disappear if we plot the surface tension as a function of the densities. This indicates that predicting the correct liquid density is a prerequisite for estimating a reliable value of the surface tension.

Since the SKS model gives a better prediction of general properties at coexistence for the long-chain alkanes [4, 29], we focus on this model for a comparison with experimental data.

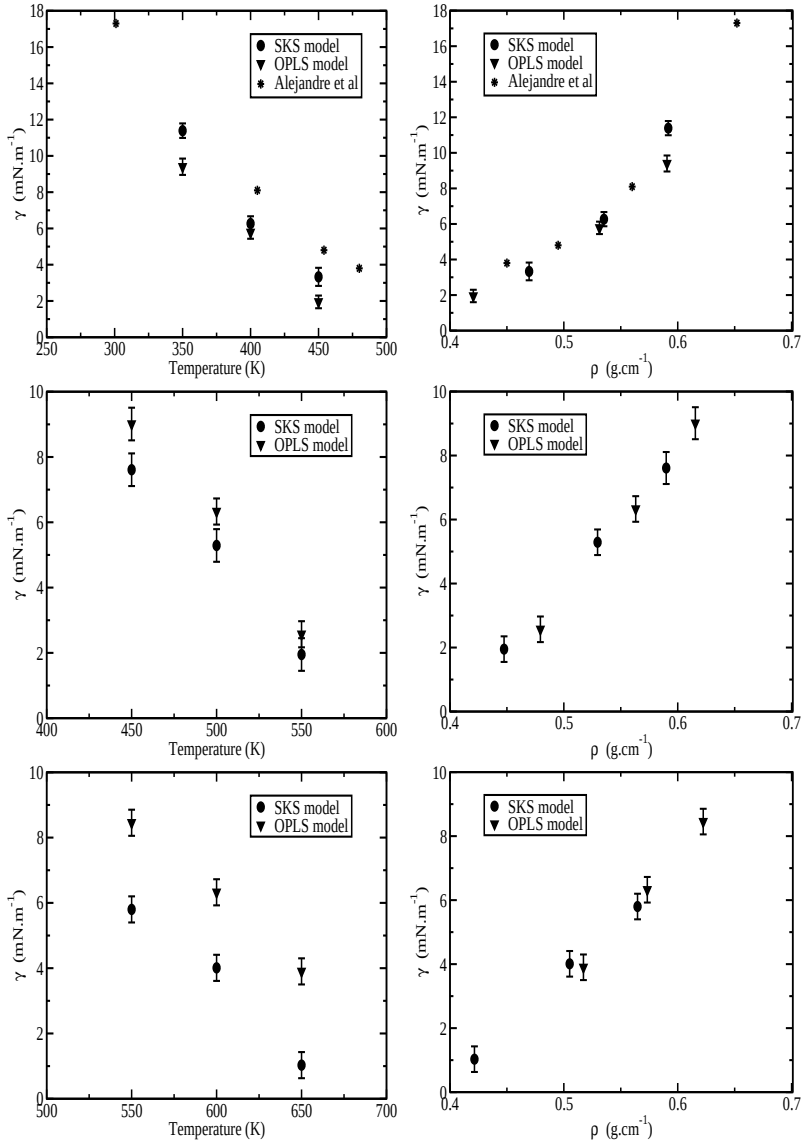


Figure 2.4: *Surface tension $\gamma$ versus the temperature (left), and density $\rho$ (right). $C_6$ (top), $C_{10}$ (centre) and $C_{16}$ (bottom), at coexistence.*

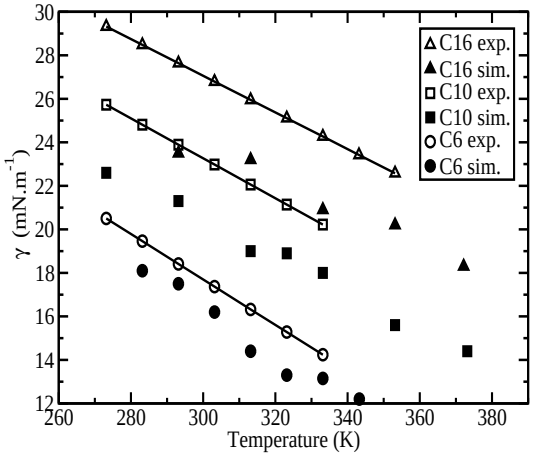


Figure 2.5: *Surface tension $\gamma$ versus the temperature: comparison of results obtained from the simulations using the SKS model (solid symbols) with experimental data (lines and open symbols) [22, 23].*

In figure 2.3 it is shown that the simulations underestimate the liquid densities at these conditions. Figure 2.5 shows that plotted versus $T$ the surface tension of the alkanes is underestimated by about 15% compared to experimental results, independently of the temperature and the length of considered alkanes.

## 2.4 Concluding remarks

In this chapter we have computed liquid densities and the surface tension of various linear alkanes at various temperatures. For longer alkanes, the computed liquid densities confirm that they are better described by the SKS model than the OPLS model at high temperatures. At lower temperatures, the agreement between experimental and computed densities from the SKS model increases with the length of the linear alkanes.

The density prediction is a major parameter in surface tension calculations. Differences observed between the SKS and OPLS models in the critical temperature and liquid density predictions are cancelled when the predicted surface tension values are plotted as a function of the liquid density. At low temperatures, comparison with experimental data shows that the surface tension is underestimated by approximately 15%.

Our simulations show that to predict the surface tension at a given tem-

perature correctly, it is very important to use a model that predicts the density of the liquid phase at the given conditions sufficiently accurately. For example, the SKS model and the OPLS model give very similar results for the surface tension as a function of the liquid density. Therefore, if a given model does not predict the liquid density correctly such a model has very limited value for predicting the surface tension.

## 2.5 Appendix: Surface tension calculation

We have used for this calculation a method described in literature [30, 31].

From the particle coordinates and the forces acting upon particles, we have computed the pressure profile along an axis perpendicular to the surface, and calculated the surface tension (which corresponds to the interfacial tension in the case of an interface). The pressure profile, which cannot yet be measured from experiments, will give an insight on the lateral pressure occurring in a membrane, and can be related to the properties specific to the composition of the membrane. The pressure profile calculation is detailed below.

For a surface normal to the $z$ axis, the surface tension $\gamma$ is proportional to the integral of the difference between the normal $P_N(z)$ and tangential $P_T(z)$ components of the pressure tensor:

$$\gamma = \frac{1}{2}\int_{-L_z/2}^{+L_z/2} \mathrm{dz}\,[\mathrm{P_N(z)} - \mathrm{P_T(z)}]\,, \tag{2.6}$$

where $\frac{1}{2}$ is a correction factor when the simulation boxes contain two surfaces. The components of the pressure tensor are obtained as a function of the position along the $z$ axis using the Irving and Kirkwood definition [30, 31]:

$$\begin{aligned}\mathrm{P_T(z)} &= \rho(z)k_BT - \frac{1}{A}\left\langle \sum_i \sum_{j>i} \frac{(x_{ij}^2 + y_{ij}^2)}{2r_{ij}} \frac{\mathrm{d}U_(r_{ij})}{\mathrm{d}r_{ij}} \frac{1}{|z_{ij}|} \right. \\ &\quad \left. \times\theta\left(\frac{z - z_i}{z_{ij}}\right)\theta\left(\frac{z_{ij}}{z_j - z}\right)\right\rangle, \end{aligned} \tag{2.7}$$

$$\begin{aligned}\mathrm{P_N(z)} &= \rho(z)k_BT - \frac{1}{A}\left\langle \sum_i \sum_{j>i} \frac{z_{ij}^2}{r_{ij}} \frac{\mathrm{d}U(r_{ij})}{\mathrm{d}r_{ij}} \frac{1}{|z_{ij}|} \right. \\ &\quad \left. \times\theta\left(\frac{z - z_i}{z_{ij}}\right)\theta\left(\frac{z_{ij}}{z_j - z}\right)\right\rangle, \end{aligned} \tag{2.8}$$

where $\rho(z)$ is the atomic density profile along the $z$ direction, $k_B$ is Boltzmann's constant, $T$ is the temperature, $A = L^2$ is the area of one surface, $x_{ij}$, $y_{ij}$, and $z_{ij}$ are the $x$, $y$, and $z$ components of the distance $r_{ij}$ between atoms $i$ and $j$, respectively, $\langle \cdots \rangle$ denotes the canonical ensemble average, $U_{\text{int.}}$ is the potential energy, and $\theta(z)$ is the Heaviside step function. Practically, the components of the pressure tensor are computed by dividing the simulation box into $N$ slabs, parallel to the $xy$ plane, and the contribution of each interaction between atoms $i$ and $j$ (including bond constraint forces from the SHAKE algorithm) is distributed in the involved slabs, i.e., slabs in which the particles $i$ and $j$ reside and slabs in between [32]. The contribution from electrostatic interactions, when taken into account, is computed from a coulombic expression.

It has been acknowledged that the position of the surface of tension $z_s$:

$$z_s = \frac{1}{\gamma} \int_0^{+L_z/2} \mathrm{d}z \, z \, [P_N(z) - P_T(z)] \tag{2.9}$$

cannot be specified exactly, but lies within a correlation length from the surface position [33, 34]. In turn, the pressure profile and its location are arbitrarily set by the used definition.

# Chapter 3

# The interfacial broadening of a liquid-liquid interface*

## 3.1 Introduction

Most of the technological and biological processes occur at an interface. However the interface between two liquids is difficult to investigate [35, 36] compared to two-phase systems as liquid-solid, solid-gas, or liquid-vapour, which exhibit large discrepancies in their molecular organization and densities, allowing extensive studies by a large range of experimental methods. Interfaces between oil and water are most widely studied since these interfaces are involved in major technological processes as crude oil extraction and detergent activity [37], and serve as models of biological hydrophilic-hydrophobic interfaces such as cell membranes [38, 39].

Since many years, the analysis of the fluid interfacial organization has been both a theoretical and experimental challenge [40–49]. Recently, developments in experimental techniques (as x-ray reflectivity, diffuse surface x-ray scattering, grazing incidence x-ray diffraction and scattering, and the optical techniques) [50–54] combined with advances in molecular simulations because of improvements of computer performance, algorithms, and force fields, have dramatically extended the insight in properties of both liquid-vapour and liquid-liquid interfaces down to the molecular scale. However, bridging the gap between theoretical predictions from capillary wave and van der Waals theories [34], and simulation and experimental results, remains an exciting

*based on: J.P. Nicolas and N.R. de Souza. Molecular dynamics study of $n$-hexane–water interface: towards a better understanding of the liquid-liquid interfacial broadening. *Journal of Chemical Physics*. In press.

challenge.

The scope of this chapter is to study the molecular organization and properties of the liquid-liquid $n$-hexane–water interface and to compare them with the prediction from capillary wave theory. This leads us to a new definition of the correlation length, commonly used as a parameter in the roughness calculation. For an ordered interface, the amplitude of the capillary waves is reduced, possibly by the intermolecular interactions involving both the two liquid bulks and the interface.

## 3.2 Method and theory

### 3.2.1 Molecular dynamics

An all-atom model was employed to describe molecules at an atomic scale using the potential energy parameter set PARM27 from the CHARMM package [55]. The interactions include non-bonded dispersive and coulombic interactions, torsion, bond bending, and vibrational potentials. The TIP3P water model [56] was used and covalent bonds involving hydrogen were held fixed with the SHAKE algorithm [18]. Electrostatic interactions were computed using the Smooth Particle Mesh Ewald method [57]. We have prepared the simulation models as follows. Beforehand, a single box containing hexane molecules at the appropriate liquid density has been equilibrated. After this, we have built our complete simulation box by the addition of two boxes of vacuum on each side along the $z$ axis. We have relaxed the resulting box containing two liquid-vacuum interfaces parallel to the $xy$ plane. Finally, we have filled the empty volume by water molecules to reach the appropriate liquid density. In such a way, the system contains 448 hexane molecules, and about 3000 molecules of water, thus approximatively 18 000 atoms in a box of dimensions $L \times L \times L_z$ in the $x$, $y$, and $z$ directions respectively, with $L = 45$ Å, $L_z \approx 95$ Å, and the volume of each bulk phase is approximately equivalent. Consequently, the simulation boxes are large enough in the $z$ direction to avoid interactions between interfaces, and thus a dependence on $L_z$ of the interfacial width [58].

Molecular dynamics computer simulations were carried out using the DLPOLY package [59]. Our calculations were performed in the NVT ensemble [60], i.e., with constant temperature, volume, and number of particles. The equations of motion were solved using the Verlet Leapfrog integration algorithm [2] and simulations were run with periodic boundary conditions. For the van der Waals terms, calculations were performed using a cutoff radius of 12 Å. The liquid-liquid systems have been equilibrated during 100 000 steps,

with a time step of 2 fs, at four different temperatures: 283, 303, 323, and 343 K. During equilibration, the density profile and energy convergence of the system have been monitored. For the present study, we have run a simulation during 2 ns and recorded the dynamics of the system by accumulating coordinates at intervals of 0.4 ps during two periods of 0.4 ns.

### 3.2.2 Interfacial ordering and width

The water molecule by definition is a planar molecule. Its orientation is fully described by two orthogonal unit vectors: $\vec{dip}$, parallel to the dipole moment, and $\vec{n}$, perpendicular to the molecular plane. The $n$-hexane orientation is represented in this study by the longest principal axis of the molecule's ellipsoid of inertia, $\vec{e}$. We have computed the molecular order parameter:

$$S(z) = \frac{1}{2}\langle 3\cos^2\theta(\mathrm{z}) - 1\rangle, \tag{3.1}$$

where $\theta$ is the angle between the vector $\vec{dip}$, $\vec{n}$ or $\vec{e}$ and the interface normal vector.

Thermal fluctuations broaden a bare (sharp) interface to a width $\sigma_{CW}$ as described by capillary wave theory [34,40]. This fluctuating bare interface is broadened (dressed) by an intrinsic width $\sigma_0$ [34,36,61]. Thus the interfacial roughness, or equivalently the total interfacial width $\sigma$, is a combination of those two components:

$$\sigma^2 = \sigma_0^2 + \sigma_{CW}^2, \tag{3.2}$$

$$\sigma_{CW}^2 \equiv \frac{k_\mathrm{B}T}{4\pi^2\gamma}\int_{q_{max}}^{q_{min}} \frac{1}{q^2 + 2a^{-2}}\mathrm{d}^2q, \tag{3.3}$$

where $q$ represents the in-plane capillary waves, $\gamma$ is the interfacial tension, $a$=$2\gamma/mg\Delta\rho$, $\Delta\rho$ is the mass density difference between the two phases, and $g$ is the gravitational acceleration.

The existence of capillary waves and their theoretical justification in both liquid-liquid and liquid-vapour systems is commonly accepted [35,36,54]. In computer simulations, from $q_{min}$ which corresponds to $2\pi/L$ and $q_{max}$ defined as $2\pi/\xi$ (where $\xi$ is a correlation length), the capillary roughness expression 3.3 becomes [34,35]:

$$\sigma_{CW}^2 = \frac{k_\mathrm{B}T}{4\pi\gamma}\ln\frac{1 + 2(\pi\mathrm{a}/\xi)^2}{1 + 2(\pi\mathrm{a}/\mathrm{L})^2}, \tag{3.4}$$

Equation 3.4 shows that in the thermodynamic limit (the area $A = L^2 \rightarrow \infty$), the interfacial width diverges as $(-\ln g)^{1/2}$ if $g \rightarrow 0$. For a microscopic system such as the one considered in computer simulations, $\xi^2 \ll a \gg L^2$, so the expression 3.4 becomes:

$$\sigma_{CW}^2 = \frac{k_B T}{4\pi\gamma} \ln \frac{L^2}{\xi^2}, \tag{3.5}$$

Despite the correlation length is defined as the shortest distance between two particles such as their motions are not correlated, it is often taken as either a molecular diameter or length. Since a liquid-liquid interface is formed of two correlated surfaces in close "contact", the relevant correlation length is expected to be an average of those characteristic of the two molecular species (water and hexane in our case). Computer simulation studies of the dependence of $\sigma_{CW}$ on $L$ agree apparently with the logarithmic behaviour in formula 3.5 (see for example [62][†]).

In the recent literature on simulations and experiments [36, 63, 64], the intrinsic width $\sigma_0$ is less well established. This comes in part from the difficulty of independently evaluating $\sigma_0$ and $\sigma_{CW}$ [61]. In experiments far from criticality, for most liquid-vapour interfaces $\sigma_0^{liq-vap} \approx 0$ because $\sigma_{CW}$ alone accounts for $\sigma$. Consistently with $\sigma_0^{liq-vap} \approx 0$, the liquid-vapour density profiles $\rho(z)$ derived from atomic positions are best fitted with a form $\psi$ based on the error function [‡]:

$$\psi(z) = \frac{1}{2}\left(\left(\rho^{liq} + \rho^{vap}\right) - \left(\rho^{liq} - \rho^{vap}\right) \mathrm{erf}\left[\frac{(z - z_0)}{\sigma\sqrt{2}}\right]\right), \tag{3.6}$$

with:

$$\mathrm{erf}(z) \equiv \frac{2}{\sqrt{\pi}} \int_0^z e^{-t^2} dt \tag{3.7}$$

where $\rho^{liq}$ and $\rho^{vap}$ are the respective bulk densities of the liquid and vapour phases, $z_0$ the position of the Gibbs' dividing surface, and $\sigma$ the interfacial width [62]. The width $\sigma$ obtained from the fit is directly proportional to the "90-10" width, defined as the width of the interfacial domain where $0.1\rho_{bulk} < \rho(z) < 0.9\rho_{bulk}$, by the relation $w_{90-10} = 1.82\sqrt{2}\sigma$.

[†] In [62], the authors explicitly set $\sigma^2 = \sigma_{CW}^2 + \sigma_0^2$, but do not provide any estimation of the intrinsic width.

[‡] Sides *et al.* compare the relative merits of erf and tanh for $\psi$, and conclude in favour of the former when thermal fluctuations are dominating [62].

Immiscible liquid-liquid interfaces seem to allow an alternative definition for $\sigma_0$ [64]. It is well known that for these the two Gibbs' dividing surfaces do not coincide, such that a depletion is present at the interface. This is unambiguously revealed as a dip in the normalized total density profile $\varphi(z) = (\rho^A(z)/\rho^A) + (\rho^B(z)/\rho^B)$, where $\rho^A$ and $\rho^B$ are the bulk liquid densities of the two species $A$ and $B$. One approach consists in defining the intrinsic width as the distance between the Gibbs' surfaces of each component, $\sigma_0^{liq-liq} = \left|z_0^A - z_0^B\right|$ [64]. This corresponds to the assumption of the direct relation between the depletion and the intrinsic width $\sigma_0^{liq-liq}$. Keeping in mind $\sigma_0^{liq-vap} \approx 0$, the interpretation of the definition is as follows: place two immiscible fluid phases "in contact", the equilibrium distance between their two bare surfaces is then determinated by van der Waals, electrostatic, and intermolecular attractive and repulsive interactions. Furthermore, the minimum of $\varphi$ is for $z = z^{interface}$, the Gibbs' dividing interface.

Obviously, the total density profile can be written as the sum of $\rho^A(z) + \rho^B(z)$ and be described accurately by:

$$\psi_{total}(z) = \frac{1}{2}\left(\left(\rho^A + \rho^B\right) - \left(\rho^A - \rho^B\right)\mathrm{erf}\left[\frac{(z - z_0)}{\sigma_{total}\sqrt{2}}\right]\right), \tag{3.8}$$

This is true as long as $\sigma_0^{liq-liq}$ is small compared to the interfacial widths for $\rho^A(z)$ and $\rho^B(z)$, and $\rho^A \neq \rho^B$.

Also, a composition profile can be used to characterize the interface:

$$\phi(z) = \frac{(\rho^A(z)/\rho^A) - (\rho^B(z)/\rho^B)}{(\rho^A(z)/\rho^A) + (\rho^B(z)/\rho^B)}, \tag{3.9}$$

By construction its midpoint coincides with $z^{interface}$. Irrespective of the depletion width and relative liquid densities, it is again well fitted by a relation similar to 3.6 or 3.8, with a width parameter $\sigma_{comp}$.

## 3.3 Results

### 3.3.1 Molecular ordering

Figure 3.1 shows the density profile derived from atomic positions at 303 K, with two sharp water–hexane interfaces. At this temperature, the simulated bulk densities are in good agreement with the corresponding experimental densities. As the temperature increases, the hexane liquid density is overestimated, by approximately 4.5% at 343 K, its boiling temperature. Inversely, the water density is underestimated to a similar extent at high temperatures. Such small discrepancies suggest that the set of parameters used in our simulations may not be optimal for high temperatures.

Figure 3.2 shows the normalized total density profiles $\varphi(z)$ close to the interface, which position is taken from the fit of the composition profile $\phi(z)$. The oil phase presents a slight layering, compared to the water phase which flattens immediately beyond the interface region. Those normalized density profiles evidence clearly a depletion at the interface, characteristic of an interface between two immiscible fluids.

Figures 3.3 and 3.4 give the molecular order parameters of hexane and water as a function of their distance from the interface. From the relation 3.1, we see that the order parameter is equal to $-0.5$ when the considered vector is parallel to the interface, is equal to 1 when the vector is normal to the interface, and 0 represents a random distribution (or a distribution centred on 54 degrees). From these two graphs, we see that both phases possess a degree of ordering extending from about 7 Å in the bulk phase to about 4 Å in the other phase.

At the interface, hexane molecules have a preferential orientation parallel to the interface (from about 65 degrees at 283 K to 60 degrees at 343 K, relative to the interface normal). There, the water dipoles adopt the same orientation as hexane molecules, but this orientation is conserved by the water molecules far into the oil side. The normal vector orientation has a different behaviour with a maximum value at the interface (corresponding to a preferential angle of about 50 degrees) and an increasing disorder as the molecules are located deeper in the oil region. This global orientation of water molecules at the interface with the oil phase is in agreement with results reviewed by Pratt and Pohorille [38].

At a distance of $4 - 7$ Å from the interface, the hexane curves display a slightly positive value of the order parameter, unlike the water curves. This difference in the profiles might be related to the stiffness and the length of the hexane molecule compared to the water molecule.

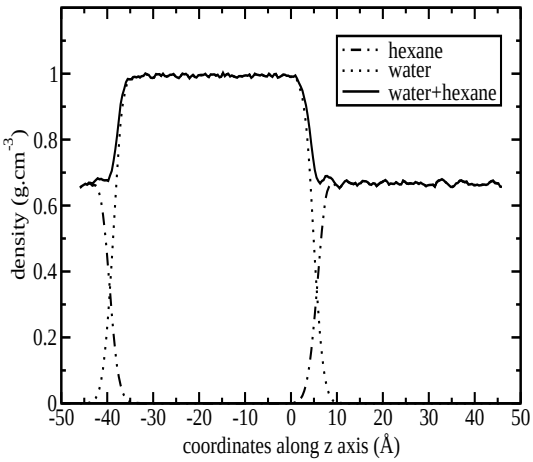


Figure 3.1: *Atomic density profiles at* 303 *K for water* $\rho^w(z)$ *(dotted), hexane* $\rho^h(z)$ *(dashed), and water+hexane* $\rho^h(z) + \rho^w(z)$ *(solid line).*

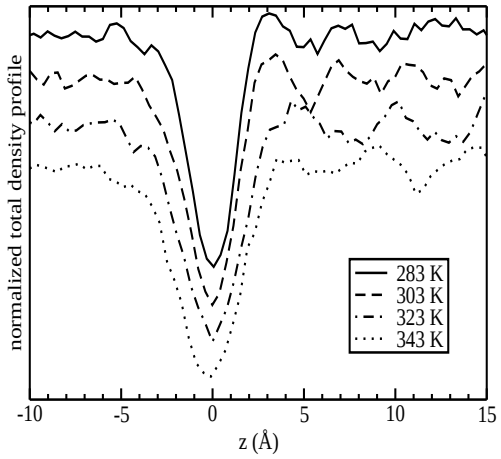


Figure 3.2: *Normalized density profiles* $\varphi(z)$ *at one interface as a function of the distance from the interface (see the text for the calculation of the interface position), at 283, 303, 323, and 343 K. The oil phase corresponds to the positive values of* $z$*, and the water phase to the negative values.*

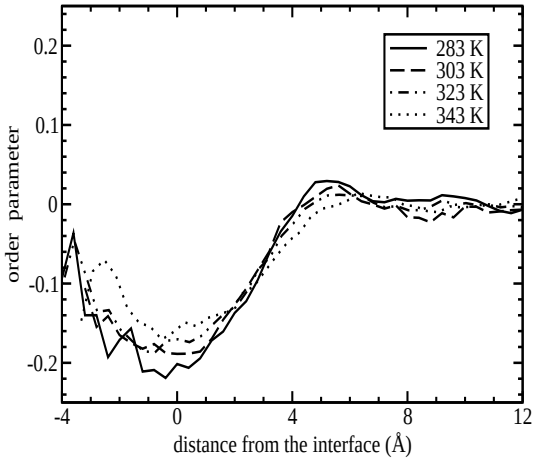


Figure 3.3: *Order parameters for hexane molecules as a function of their distance from the interface at 283, 303, 323, and 343 K. The hexane phase corresponds to positive values of the distance. Data are averaged over the two interfaces. On the left side, the curves are noisier due to a smaller statistical accuracy.*

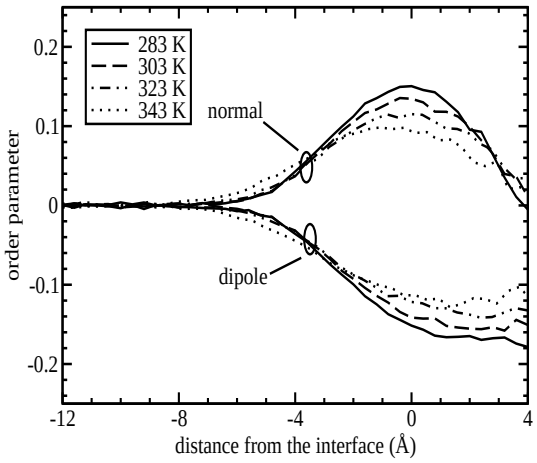


Figure 3.4: *Order parameters for water molecules as a function of their distance from the interface at 283, 303, 323, and 343 K. The water phase corresponds to negative values of the distance. Both contributions from the dipole and normal vectors are reported. Data are averaged over the two interfaces. On the right side, the curves are noisier due to a smaller statistical accuracy.*

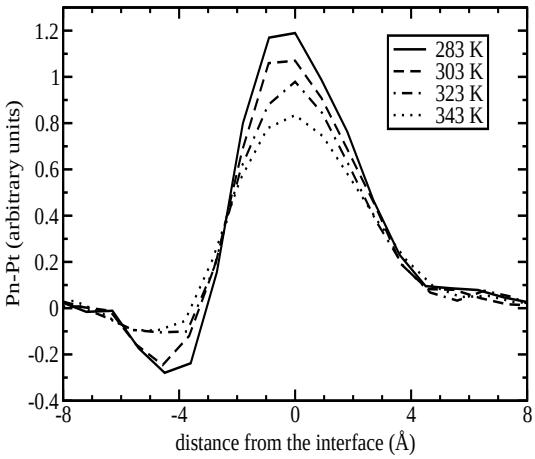


Figure 3.5: *Pressure profile $P_N - P_T$ as a function of temperature. The water phase corresponds to negative values of the distance and the hexane phase to the positive ones.*

To complete the description of the interfacial organization, we have computed the orientation of the projection of the hexane molecular director in the interfacial plane. No preferential orientation is noticeable, implying that hexane molecules are disordered in the plane of the interface (data not shown).

For both the hexane and the water molecules, increased temperature reduces the ordering at the interface. This can be related to an alteration of the hydrogen bond network for the aqueous phase and an enhancement of the dynamics of molecules, as the temperature increases.

### 3.3.2 Interfacial tension

Figure 3.5 reports the pressure profiles $P_N - P_T$ as a function of the temperature. The pressure profile is zero in the two bulk phases. At the interface, the charged water molecules are ordered. This peculiar organization yields a polarization of the interfacial molecular layer, corresponding to a negative pressure profile. Inversely, the oil phase, with a low electron density and a reduced ordering (molecules are only ordered parallel to the interface, with no in-plane order), has no electrostatic contribution to the pressure profile.

As the ordering of molecules at the interface, the interfacial tension (from relation 2.6) decreases with the temperature. Computed values of interfacial tension are compared with experimental results $\gamma_{exp}$ [53] in Table 3.1. Our results are about $9 - 10\%$ smaller than experimental results, except for the

| T (K) | $\sigma^w$ | $\sigma^h$ | $\sigma^{h-w}_{total}$ (Å) | $\sigma^{h-w}_{comp}$ | $\sigma^{h-w}_0$ (Å) | $\sigma^{h-w}_{CW}$ | $\gamma_{sim}$ ($mN.m^{-1}$) | $\gamma_{exp}$ | $\xi'$ (Å) | $\xi''$ |
|---|---|---|---|---|---|---|---|---|---|---|
| 283 | 1.59 | 1.46 | 1.03 | 1.43 | 0.52 | 1.68 | 53 | 51.4 | 22.9 | 9.9 |
| 303 | 1.67 | 1.53 | 1.22 | 1.48 | 0.54 | 1.87 | 46 | 50.0 | 19.7 | 12.1 |
| 323 | 1.82 | 1.72 | 1.39 | 1.61 | 0.61 | 1.99 | 43 | 48.1 | 17.4 | 11.6 |
| 343 | 1.95 | 1.79 | 1.52 | 1.70 | 0.64 | 2.10 | 41 | 46.4* | 15.9 | 11.6 |

Table 3.1: *Fitted surface widths ($\sigma^w$ and $\sigma^h$), interfacial widths ($\sigma^{h-w}$, $\sigma^{h-w}_{total}$ and $\sigma^{h-w}_{comp}$), intrinsic width ($\sigma^{h-w}_0$), computed capillary wave width ($\sigma^{h-w}_{CW}$), experimental ($\gamma_{exp}$) [53] and computed ($\gamma_{sim}$) interfacial tensions, and corrected correlation lengths ($\xi'$ and $\xi''$). The computed interfacial tensions are defined with an error bar of $\pm 1.6 mN.m^{-1}$. (* extrapolated value from Zeppieri results [53])*

lowest temperature where the computed interfacial tension is greater than the experimental interfacial tension. For this latter case, the representation of the system at the lower temperature may not reproduce the experimental liquid-liquid interface with an expected accuracy. The estimation of the interfacial tension for a liquid-liquid system is improved compared to the calculation of the surface tension of a liquid-vapour system done with the same method [65]. This is likely due to the consideration of the electrostatic term in the force field. It is worth noticing that our calculation, which is performed without any long range correction, yields an underestimation independent of the system studied [65, 66], while calculations with a long range correction yield an underestimation of the interfacial tension for short alkanes and an overestimation for the longer ones [63].

### 3.3.3 Interfacial width

The correlation length $\xi$ is a parameter for the interfacial width resulting from thermal fluctuations. As reported above, while its definition is well established, its choice is not discussed in the literature and, as mentioned, $\xi$ is always estimated as/from either the diameter or the length of one of the two molecules. Since $\xi$ is located in the logarithm of the relation 3.5, one might consider that its order of magnitude is sufficient to estimate correctly the interfacial width $\sigma_{CW}$.

Still, Akino and coworkers [67] pointed out that for a nematic phase of ellipsoid molecules placed at an interface, the amplitude of capillary waves in a direction parallel to the ellipse director is smaller compared to the amplitude of the waves perpendicular to the molecular axis. Consequently, we assume

that the larger wave amplitude, responsible for the interfacial widening, is related to the molecular diameter and not the molecular length. We have chosen $\xi$ as equal to the hexane molecular diameter, thus approximately 4 Å . This value is close to the value of the water molecular diameter, 3.2 Å. The capillary widths obtained from this choice of $\xi$, and using our computed values of interfacial tension, are reported in Table 3.1.

We have fitted to an error function (see formulas 3.6 and 3.8) the density profiles related to the hexane, the water, the total, and the composition density profiles (as defined by equation 3.9). In these formulas, we fixed the bulk density parameters and fitted the interface parameters: $z_0$ and $\sigma$. Figure 3.6 shows the difference between the fitting curves and the corresponding density profiles. This difference allows both a qualitative and quantitative estimation of the goodness of the fits. In the region delimited from $-5$ Å to $+10$ Å the plots present some small features which are not centred on the Gibbs' dividing surface but mainly occur at the hexane surface. They originate from the features observed on the hexane density profile at the interface (Figure 3.1). Outside this region, the difference corresponds to microscopic fluctuations of the density profile. The fitted $\sigma$ parameters are reported in Table 3.1. Strikingly, $\sigma_{CW}$ is consistently larger than $\sigma_{total}$ by 50% and $\sigma_{comp}$ by 25%. This trend is also present in other works, see for example [68]. This situation precludes validating directly the capillary wave theory model of the interface, and a fortiori the hybrid model (relation 3.2).

The intrinsic width $\sigma_0^{liq-liq}$ corresponds to about one third of $\sigma_{total}$ (see Table 3.1). Together with the small deviations observed on figure 3.6, this justifies using formula 3.8 to represent the total density profile. The normalized density profiles give "90-90" widths fully consistent with $\sigma_0^{liq-liq}$. It is worth noticing that the intrinsic width as computed in this article depends on the temperature and is not the width computed between the two inflection points of the normalized density profiles [69].

## 3.4 Discussion

To the best of our knowledge, there has been no published account of simulation studies aiming at verifying accurately the interrelations between $\sigma_0$, $\gamma$, and $\xi$ for liquid-liquid interfaces. Therefore the following discussion attempts to resolve the disagreement with capillary wave theory.

While questionable, the use of the experimental interfacial tension instead of the computed value cannot explain the amplitude of the observed discrepancy. Rather, we focus on the order at the interface, which has been

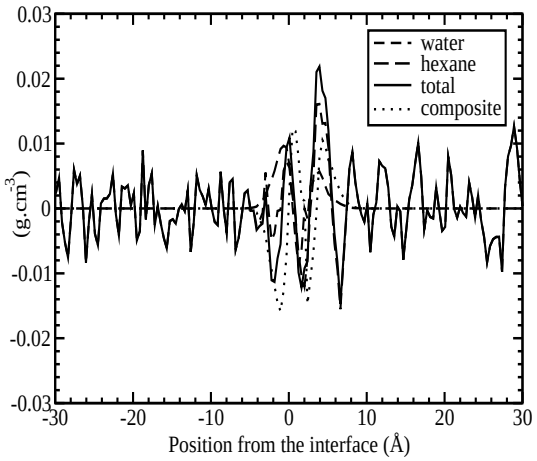


Figure 3.6: *Difference between $\rho^h(z)$, $\rho^w(z)$, $\rho^h(z) + \rho^w(z)$, and $\phi(z)$, density profiles, and their fitting function at a temperature of 303 K. The interfacial position has been determined from the fit of $\phi(z)$.*

found in other simulations of alkane-water interfaces [38,63,68,70,71]. From their X-ray scattering experiments, Schlossman and coworkers do not exclude such an interfacial organization [72,73]. While it involves both surfaces, one might expect a screening of certain capillary modes. In the case of a nematic interface [67], this screening is observable in the direction parallel to the molecular director. In the case of the hexane–water liquid-liquid system, since the hexane molecules are disordered in the plane at the interface, the screening occurs isotropically in-plane, yielding a dramatic reduction in the effect of the thermal fluctuations.

Consequently, one needs to specify better the parameter $\xi$ for ordered interfaces. Two conventions coexist in the literature. Concerning thin films located at the interface (in fact similar to the interfacial layer of a pure liquid) the correlation length refers to the transverse correlation length [58], while for an interface between two ideal liquid phases, this correlation length is taken as the bulk correlation length. In our case, molecular motions at the interface result from two kinds of interactions, those from the underlying bulk (more accurately from the two bulks in the case of an interface) and those between the molecules making up the interface. Thus, the correlation length must correspond to a combination of the two definitions given above. In order to estimate a corrected value of the correlation length, we have fitted to $\sigma_{total}$ (resp. $\sigma_{comp}$) the prediction from relation 3.2 with only $\xi \equiv \xi'$ (resp. $\xi''$) as a

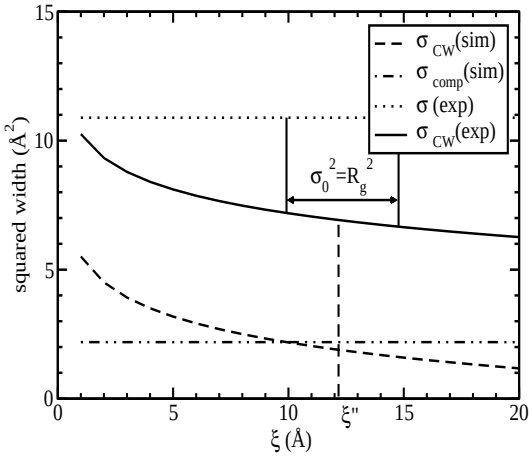


Figure 3.7: *Variation of* $(\sigma_{CW}^{h-w})^2$ *against the correlation length* $\xi$*, at* 303 *K. The bottom curve uses an upper cutoff* $q_{max} = 2\pi/L$ *to describe our simulations. The top curve uses a cutoff* $q_{max} = 2\pi/L_{exp}$ *to describe the experiments of Schlossman and coworkers [72]. Horizontal lines refer to the observed* $\sigma_{comp}^{h-w}$ *in simulation and* $\sigma_{total}$ *in experiment. Below* $\xi = 10$ *Å the capillary wave model cannot be consistent with the simulated* $\sigma$*.*

free parameter, using the computed value of $\sigma_0^{liq-liq}$ reported in the table 3.1. The resulting values for $\xi'$ and $\xi''$ are given in the same table. $\xi'$ shows a decrease from 19.7 Å (less than half of the simulation box) at 303 K, to 15.9 Å at 343 K, in keeping with the behaviour of $\sigma_{total}$. On the other hand, $\xi''$ is almost constant in this range of temperatures. Because the data at the lowest temperature might not represent accurately the experimental interface, it is difficult to conclude on the significance of the correlation lengths at 283 K relative to those of the higher temperatures.

It is interesting to use $\xi'$ and $\xi''$ for predicting measured capillary widths. For this purpose, we use $\gamma_{exp}$ [53] and $L_{exp}$ [74] in relation 3.5: the values of $\sigma_{CW}$ obtained together with the corrected correlation lengths are then smaller than the experimental widths for hexane–water measured by X-ray scattering in reference [74]. The difference corresponds likely to some intrinsic width $\sigma_0^{liq-liq}$. Ours is far too small to recover the observed width. Taking for $\sigma_0^{liq-liq}$ the radius of gyration of the alkane [72] seems to work better ($R_g = 2$ Å for hexane). The situation is summarized in figure 3.7, at the temperature 303 K close to experimental conditions of [74].

## Concluding remarks

A careful study of the ordered interface between two immiscible fluids reveals the disagreement between the actual interfacial width and its prediction from the capillary wave theory. The discrepancy can be resolved by using a correlation length consistent with the molecular organization at the interface. So improved, our prediction is compatible with experimental results. Further studies require to fully characterize the intrinsic width, so as to provide a firmer basis to our hypothesis.

# Part B

# Surfactant activity

# Chapter 4

# Surfactin: a "chimeric" peptide*

## 4.1 Introduction

Surfactin is an amphiphilic lipopeptide produced by various strains of *Bacillus subtilis* [75] and consists of a heptaptide headgroup with the sequence Glu-Leu-*D*Leu-Val-Asp-*D*Leu-Leu linked to a $RC_{14-15}$ $\beta$-hydroxy fatty acid [76] and closed by a lactone ring. Surfactin is a powerful biodegradable surfactant lowering water surface tension from 72 to $\sim$ 30 mN/m at concentrations of $\sim$ 10 $\mu$M [77, 78]. At very low concentrations it forms large micelles and the critical micellar concentration of the different analogues is of the order $10^{-5}$ M [77]. Besides its interfacial properties, surfactin exhibits several biological activities: antibacterial [79, 80], hemolytic [81], antiviral [81, 82], and antitumoral [83]. Surfactin interacts with membranes [84], initiates lipid phase transitions [85], and membrane destabilization [86]. Such surface and biological properties have attracted interest in the structure of surfactin and its behaviour at hydrophilic/hydrophobic interfaces.

From $^1$H-NMR studies correlated to distance geometry, energy minimization, and molecular dynamics techniques, a first three-dimensional structure for surfactin in DMSO has been proposed [87]. Two models were presented where in both cases the peptidic moiety adopts a "horse-saddle" conformation with the two hydrophilic residues pointing on one side forming a potentially binding "claw" and the five hydrophobic ones associated to the fatty acid chain pointing on the other side. The two structures differ

*based on: J.P. Nicolas. Molecular dynamics simulation of surfactin molecules at the water-hexane interface. *Biophysical Journal.* **85**, 1377–1391, 2003.

mainly with respect to their intramolecular hydrogen bonds, [NH(5)-CO(2)] and [NH(7)-CO(5), NH(4)-CO(2), NH(6)-$C_1O$] for S1 and S2 structures, respectively. Structure-activity correlation has been extensively studied during micelle formation [77, 88], by FTIR spectroscopy and circular dichroism in various solvent systems [89, 90], and at the air/water interface [91, 92] and hydrophobic/hydrophilic mimicking medium [93]. All those recent results suggest flexibility of the backbone conformational structure and several stable configurations are proposed and debated.

The purpose of our work was to explore the conformational flexibility of surfactin for various interfacial concentrations in a hydrophilic/hydrophobic medium, similar to a biological system as the lipid/water interface. In order to avoid perturbations resulting from aliphatic chain order and lipid headgroup interactions, we have mimicked this environment with an amorphous hexane/water system described at an atomic scale. Furthermore, we have computed the effect of adding biosurfactant on the interfacial tension at the oil/water interface and estimated the lateral and rotational diffusion coefficients.

## 4.2 Methodology

### 4.2.1 Molecular dynamics

#### Simulations

Molecular dynamics computer simulations were carried out using the DL-POLY package [59]. An all-atom model was employed to describe molecules at an atomic scale using the potential energy parameter set PARM27 from the CHARMM package [55]. The TIP3P water model [56] was used in all simulations. Bonds involving hydrogen were held fixed with the SHAKE algorithm [18]. Electrostatic interactions were computed using the Smooth Particle Mesh Ewald method [57]. Our simulations were performed in the NVT ensemble [60], i.e., with constant temperature, volume, and number of particles. The equations of motions were solved using the Verlet Leapfrog integration algorithm [2] and simulations were run with periodic boundary conditions. All the simulations were performed using a cutoff radius of 12 Å for the van der Waals terms.

Initially, a single protonated surfactin molecule was equilibrated in vacuum. Bonmatin has kindly provided the coordinates of the S1 and S2 heptapeptide conformers of the surfactin molecule which have been completed with a $R$-$C_{14}$ $\beta$-hydroxy fatty acid chain [76]. The analysis of those con-

formers with hydrogen bond criteria [94, 95] shows that S1 exhibit a $\beta$-turn type II' Asp(5)→Leu(2) with two hydrogen bonds CO(5)-NH(2) and NH(5)-CO(2), whilst S2 contains two reverse $\gamma$-turns centred on the $D$-residues with their respective hydrogen bond, Val(4)→Leu(2) and Leu(7)→Asp(5), and a third hydrogen bond NH(6)-$C_1$O. After this preliminary protonated structure relaxation, we have built our complete models in three steps. First, we have equilibrated a box containing two phases, liquid hexane and vacuum, with interfaces parallel to the $xy$ plane. Subsequently, surfactin molecules have been added to the box, with the fatty-acid chain inserted in the liquid hexane phase and the heptapeptide moiety at the interface. A few runs of equilibration were carried out with a very small time step, which was gradually increased until a final value of 2 fs. Finally, the boxes were filled by adding water molecules. In such a way systems were prepared containing 448 hexane molecules, 2, 4, 8, 18, 24, or 32 molecules of surfactin (corresponding to 1, 2, 4, 9, 12, or 16 molecules per interface, respectively), and about 2000 molecules of water, thus approximatively 17000 atoms. The box dimensions were $45 \times 45 \times L_z$ Å in the $x$, $y$, and $z$ directions, respectively, with $L_z \approx 93$ Å. These systems have been equilibrated for 100.000 steps, with a time step of 2 fs at a temperature of 303 K. During equilibration, density profiles and energy convergence of the system have been monitored. After equilibration, we have recorded the dynamics of the system by accumulating coordinates at an interval of 0.4 ps during two periods of 0.5 ns.

### 4.2.2 Structure analysis

#### Peptide shape and orientation

To study the dynamics of surfactin molecules as a function of interfacial concentration, we have computed: the trajectory of the centre of mass of the surfactin's head (thus, all the atoms except those of the fatty-acid chain), its lateral diffusion, and the averaged distance between the centres of mass in order to estimate the molecular area.

Figure 4.1 shows the three-dimensional structure of the surfactin molecule in which the peptide part takes the form of a "horse-saddle". This structure can be modelled by a tetrahedron, build from four atoms from the cyclopeptide backbone (see legend of figure 4.1). To characterize the shape and orientation of this horse-saddle we have introduced the vectors $\vec{S}_{top}$, $\vec{S}_{base}$, and $\vec{S}_{height}$ and the dihedral angle $\alpha_{dih.}$. The magnitude of the vectors $\vec{S}_{top}$, and $\vec{S}_{base}$ characterizes the degree of opening of the hydrophilic and hydrophobic side of the horse-saddle, respectively. The rotation of the surfactin molecule

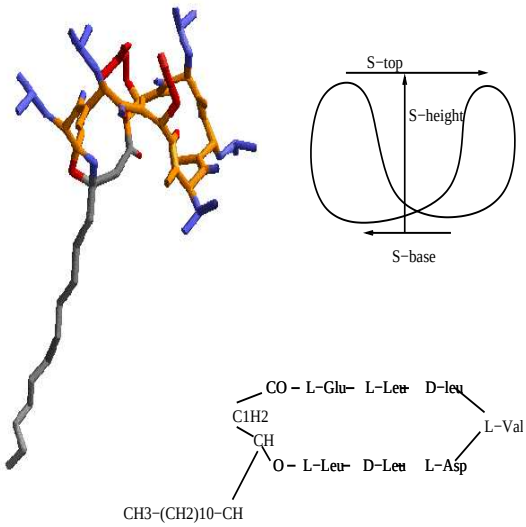


Figure 4.1: *Modelling and parametrization of the "horse-saddle" conformation of surfactin. From four atoms defining a tetrahedric structure,* $\boldsymbol{CO(5)}$, $\boldsymbol{NH(2)}$, $\boldsymbol{CH(4)}$, *and* $\boldsymbol{C_1H}$, *are defined three vectors:* $\vec{S}_{top}$*:* $\boldsymbol{CO(5)} \rightarrow \boldsymbol{NH(2)}$, $\vec{S}_{base}$*:* $\boldsymbol{C_1H} \rightarrow \alpha\boldsymbol{CH(4)}$, *and* $\vec{S}_{height}$*:* $[\boldsymbol{CO(5)}\text{-}\boldsymbol{NH(2)}] \rightarrow [\boldsymbol{C_1H}\text{-}\alpha\boldsymbol{CH(4)}]$*. The dihedral angle* $\alpha_{dih.}$ *is defined by the angle between two vectors normal to two sides of the tetrahedron, each containing three atoms* ($\boldsymbol{NH(2)}$-$\alpha\boldsymbol{CH(4)}$-$\boldsymbol{CO(5)}$) *and* ($\alpha\boldsymbol{CH(4)}$-$\boldsymbol{CO(5)}$-$\boldsymbol{C_1H}$)*, respectively.*

is described by the orientation of the $\vec{S}_{height}$ vector. In the case of a tetrahedral structure, $\vec{S}_{height}$ vector is orthogonal to the two orthogonal vectors $\vec{S}_{top}$ and $\vec{S}_{base}$. Thus, the orientation of the $\vec{S}_{height}$ vector can be defined as a sum of contributions from the vectors $\vec{S}_{top}$ and $\vec{S}_{base}$. A negative value of $\vec{S}_{height}$ orientation towards the interface corresponds to a tumbling over of the peptidic part of the surfactin molecule. The dihedral angle $\alpha_{dih.}$ characterizes the horse-saddle shape which can be modelled by a tetrahedron. It corresponds to the angle between the two vectors normal to two faces of the tetrahedron (see legend of figure 4.6). A symmetrical horse-saddle shape yields an angle $\alpha_{dih.}$ of $\sim$ 74-75 degree. A change in the sign of $\alpha_{dih.}$ corresponds to an inversion of the horse-saddle conformation, and a value close to 0 corresponds to a flat structure.

### Secondary structure

In our simulations we observe that the surfactin structure may fluctuate depending on the molecular orientation and the interfacial concentration. We have computed Ramachandran angles and hydrogen bonds (intramolecular, and intermolecular between surfactins, and with the solvent) in order to describe the secondary structure of the surfactant molecule and its flexibility, and to detect secondary structures as $\gamma$- and $\beta$-turns.

Hydrogen bonds are described from parameters specific to proteins [94, 95]. These criteria are a maximum distance of 2.5 Å between H (hydrogen atom) and A (hydrogen acceptor) and a minimum angle of 90 degrees for A$\cdots$Ĥ-D (hydrogen donor) when A, H, and D coordinates are available. Such criteria allow a complete screening of the most common hydrogen bonds found in proteins but may underestimate bonds involved in particular secondary structure motifs such as $\gamma$- and $\beta$-turns, and main-chain lateral-chain interactions. Moreover, we have extended the potential hydrogen bond acceptors to include the main-chain nitrogen atom as described in a previous theoretical study [96].

### Rotational and lateral diffusion

The lateral diffusion coefficient ($D_T$) has been obtained from the mean square displacement of the centre of mass of the peptidic moiety. At long times the diffusion coefficient is:

$$D_T = \lim_{t\to\infty} \frac{1}{2d \times t} \left\langle |\mathbf{r}(t) - \mathbf{r}(0)|^2 \right\rangle , \tag{4.1}$$

where $\mathbf{r}(t)$ is the position of the peptide centre of mass at time $t$, and $d$ the spatial dimension of the displacement. In our case, we have studied surfactant molecules remaining in the planar oil/water interface, hence, we have computed the two dimensional (translational) diffusion coefficient.

The calculation of the rotational diffusion coefficient is based on the Debye theory [97] which assumes a very diluted solution of rigid dipoles with Brownian motion rotating in nonpolar media. Application of the theory has been extended to more complex systems and good results have been obtained for protein/water systems [98]. The rotational diffusion coefficient ($D_R$) can be obtained from the relation:

$$\langle P_l[cos\theta(t)]\rangle = e^{-l(l+1)D_r t} = e^{-t/\tau_l}, \tag{4.2}$$

where $\theta(t)$ is the angle between two $\vec{S}_{height}$ vector orientations spaced in time by $t$, $P_l$ is the $l$th rank Legendre polynomial, and $\tau_l$ the rotational relaxation time associated with each of the Legendre polynomial correlation functions. For molecules undergoing Debye diffusional rotation, a plot of $1/\tau_l$ against $l(l+1)$ should be linear with a slope equal to $D_R$.

## 4.3 Results and discussion

In this section, we first analyse the behaviour of surfactin molecules at the interface through the study of density profiles and centre of mass motions of the cyclopeptide moiety. Next the secondary structure of the peptidic part is analysed, and finally, we relate our results to interfacial properties.

### 4.3.1 Behaviour at the interface

#### Density profiles

From atomic density profiles plotted in figure 4.2 *A* we observe that surfactin molecules reside at the hexane/water interface. A coordinate analysis of the terminal methyl group of the aliphatic chain (not shown) shows an anchoring of the surfactin molecule in the oil phase. For the three lower concentrations, the surfactin density is increasing with the interfacial concentration, while for the three higher concentrations, the increase of the concentration yields a widening of the surfactin density peak combined with a smoother water interface, as shown in figure 4.2 *B*. This broadening suggests that the organization of the surfactant layer has changed with surfactin molecules slightly popping out of the surfactant monolayer.

#### Centre of mass motions

The projection of the centre of mass displacement onto the plane of the interfaces is shown in figure 4.3 for low concentrations and in figure 4.4 at high concentrations. From those snapshots, we observe that molecules exhibit a gas-like behaviour with uncorrelated motions below a concentration of 4 molecules per interface, a solid-like behaviour with collective motions above a concentration of 12 molecules per interface, and a liquid-like behaviour for intermediary concentrations. This behaviour is confirmed by the study of the distance between two surfactin molecules placed at the same interface (not shown). This distance is rather constant at high concentrations but fluctuates at lower concentrations. At the concentration of 4 surfactins per

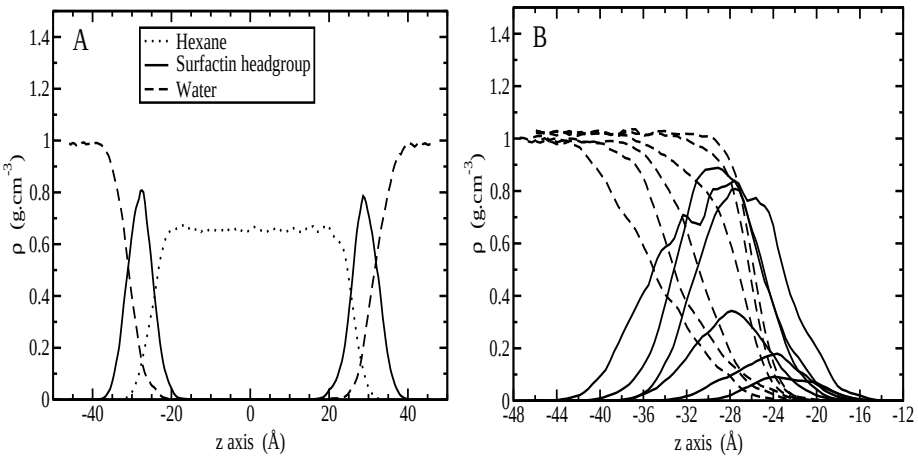


Figure 4.2: *Density profiles at 303 K, (*A*) shows hexane (dotted line), water (dashed line), and surfactin headgroup (straight line) at a concentration of 9 surfactins per interface, (*B*) shows the surfactin (straight line) and water (dashed line) profiles at one interface for the different interfacial concentrations: 16, 12, 9, 4, 2, and 1 surfactin(s) per interface, from left to right, respectively.*

interface, figure 4.3 *C*, where four molecules are located at each interface in the simulation box, few molecules are clustered. Within a cluster, molecules can be surrounded by one or two neighbouring molecules. Molecules are spaced by a minimal distance which decreases from approximatively 15 Å at a concentration of 4 molecules per interface to less than 10 Å at the highest concentration. These intermolecular distance fluctuations suggest a conformational flexibility of the peptide moiety. Intermolecular distances yield an estimation for areas per molecules of surfactin which fluctuate from 177 $Å^2$ at a concentration of 4 molecules per interface, where the interface is not completely covered by surfactant but few molecules are already in contact, to 78 $Å^2$ at the highest concentration where we observe the onset of a solid phase. Our results are similar to $A_0$ and $A_t$ molecular areas obtained from $\Pi$-$A$ isotherms [77] at pH 4.2, where the surfactin molecule is fully protonated, equal to 184 and 89 $Å^2$, respectively.

As we will demonstrate next, the properties of the surfactin molecules strongly depend on the aggregation state and their orientation.

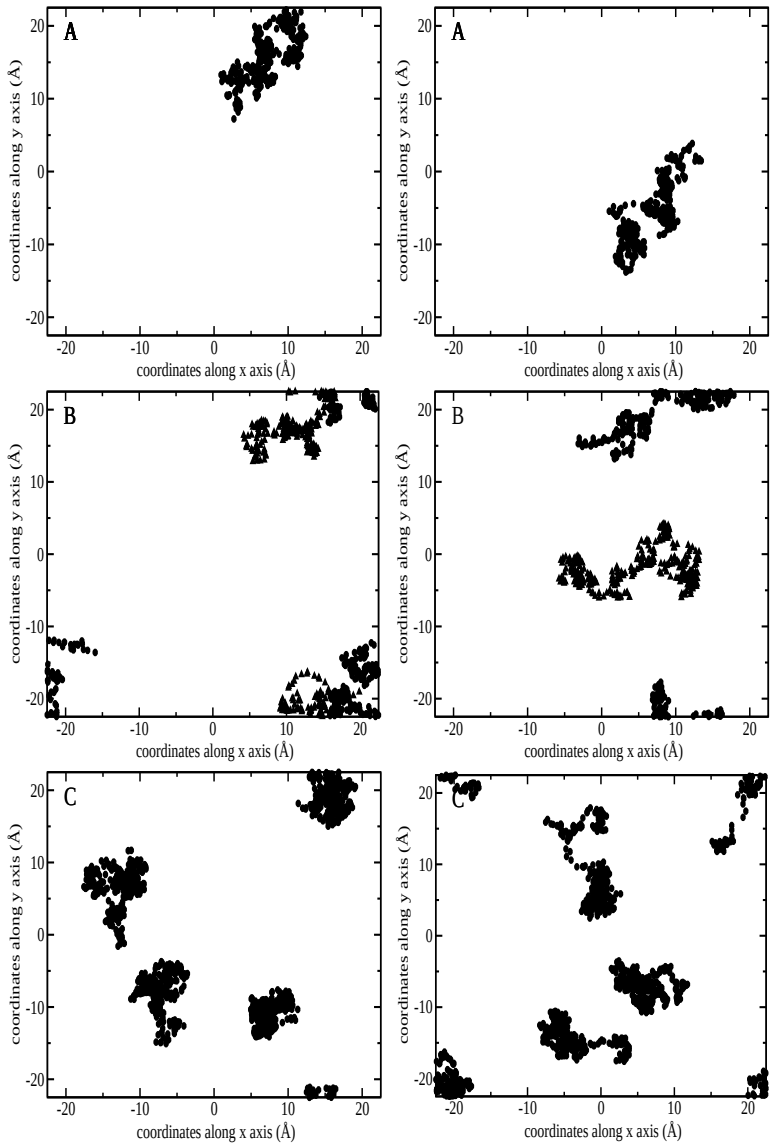


Figure 4.3: *Projection of the centre of mass of each peptidic moiety at various concentrations. Each molecule centre of mass at an interface differs by a color. Each box represents the xy plane and periodic boundary conditions have been applied on coordinates. (*A*) 1, (*B*) 2, and (*C*) 4 surfactins per interface for each interface, left figures and right figures.*

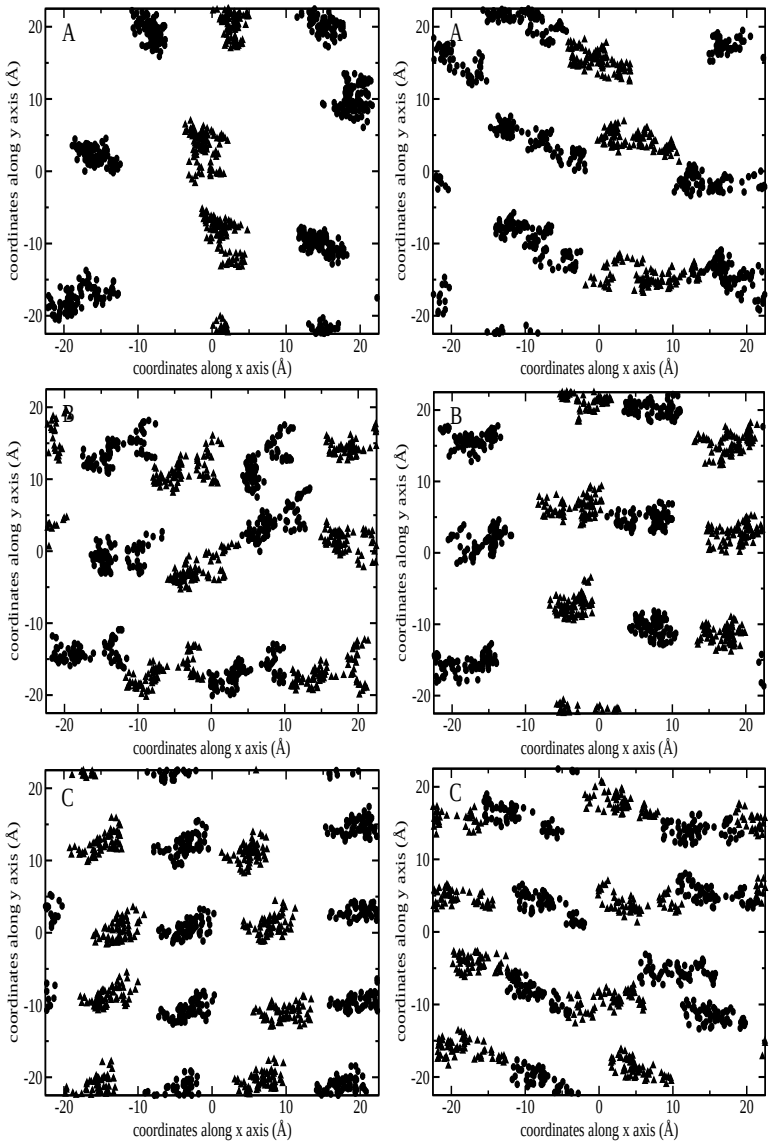


Figure 4.4: *Projection of the centre of mass of each peptidic moiety at various concentrations. (*A*) 9, (*B*) 12, and (*C*) 16 surfactins per interface for each interface, left figures and right figures.*

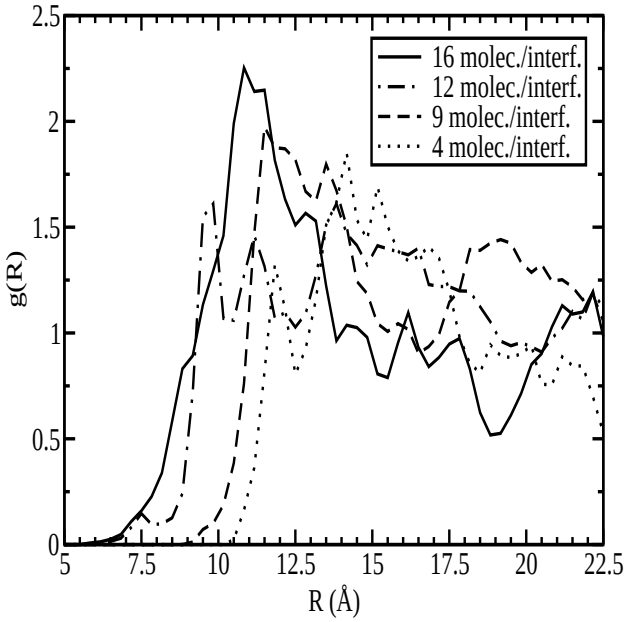


Figure 4.5: *Radial distribution function of the centre of mass of the peptidic moiety at 4, 9, 12, and 16 surfactins per interface.*

### Radial distribution functions

Figure 4.5 *A* shows the radial distribution function of the centre of mass of the peptidic part of surfactin molecules at a range of surfactin concentrations. The first peak is observed at about 12, 11.5, 9.5 and 9-12 Å at a concentration of 4, 9, 12, and 16 molecules per interface, respectively, corroborating a compression of surfactin molecules as the interfacial concentration increases. Radial distribution functions have been computed from the projection of the centre of mass coordinates onto the interface. As a consequence, molecules popping out of the interface yield minor peaks placed at distances shorter than 8 Å and contribute to a broadening of the peaks. Moreover, the radial distribution functions plotted in figure 4.5 are an average from the contributions of the two interfaces. As a consequence, at the highest concentration, the contribution from the most ordered interface is counterbalanced by the contribution from the other interface, which is less ordered (see figure 4.4 *C*), yielding a radial distribution function not representative to an ideal bidimensional solid.

### 4.3.2 Molecular shape and orientation

Figure 4.6 displays the fluctuations of the $\alpha_{dih.}$ angle related to the tetrahedral shape model of the molecule. At all surface concentrations, the angle distributions exhibit a main peak, sharp and centred on 80-85 degree at high concentrations (figure 4.6 *A*), and broader with a few other contributions which depend on the orientation of molecules and their environment at low concentrations (figure 4.6 *B*). At low concentrations, molecules can be described as clustered or free (the latter may tumble over). On the one hand free molecules not tumbled over have a rather flexible tetrahedral shape, on the other hand clustered or tumbled over free molecules exhibit a stable $\alpha_{dih.}$ angle equal to 50-55 and 80-85 degrees, respectively, as shown on figure 4.6 *C*. However, such an $\alpha_{dih.}$ angle range demonstrates that surfactin molecules at the water/hexane interface adopt a tetrahedral shape, which is similar to the compact "horse-saddle" conformation observed under particular conditions [87] where surfactin was in a DMSO solution. The amplitude of the observed dihedral angle distributions ascertains the flexibility of the secondary structure which never remains flat or adopts a reversed saddle shape.

To characterize the orientation of the molecule, i.e., the saddle up or down, we have computed the angle between $\vec{S}_{height}$ and the $xy$ plane, parallel to the two hexane/water interfaces. At high concentrations, figure 4.7 *A* shows angular distributions in a range of 15-90 degree with minor contributions below 15 degree. At 16 molecules per interface, the distribution is rather large and centred around 45 degree while at a concentration of 9 molecules per interface the distribution is made of a main peak with a mean angle value of 70 degree. When the interfacial concentration is increased, the surfactin solid-like molecules popping out of the planar interface may adopt a tilted orientation but have less freedom to tumble. Figures 4.7 *B* and *C* illustrate that for concentrations below 4 molecules per interface, molecules may tumble over. At low concentrations, the proportion of tumbled over molecules (corresponding to a negative angle value) increases inversely with the concentration. During our recorded simulations, we have observed one tumbling over motion within a few tens of picoseconds. That means that the other observed tumbled molecules have tilted during the equilibration time. Moreover, at the concentration of 2 molecules per interface, we have observed at an interface, two molecules clustered with opposite orientation, forming a kind of "dimer".

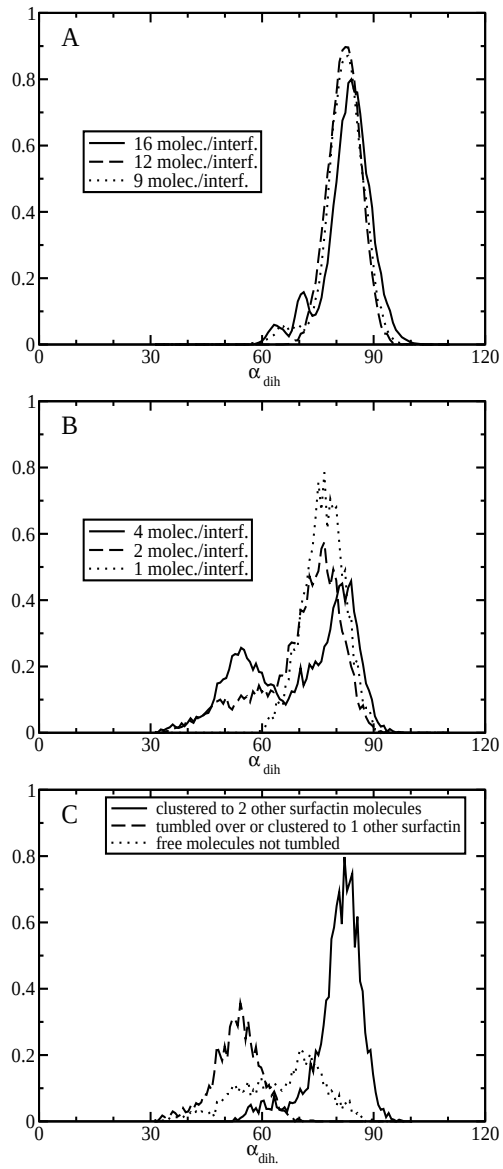


Figure 4.6: *Normalized distributions of the $\alpha_{dih.}$ angle at various interfacial concentrations. (*A*) 9, 12, and 16 surfactins per interface, (*B*) 4, 2, and 1 surfactins per interface, and (*C*) at a concentration of 4 surfactins per interface plotted with the contributions of molecules clustered with two neighbours (straight line), clustered with one neighbour, free and tumbled over (dashed line), and free molecules (dotted line).*

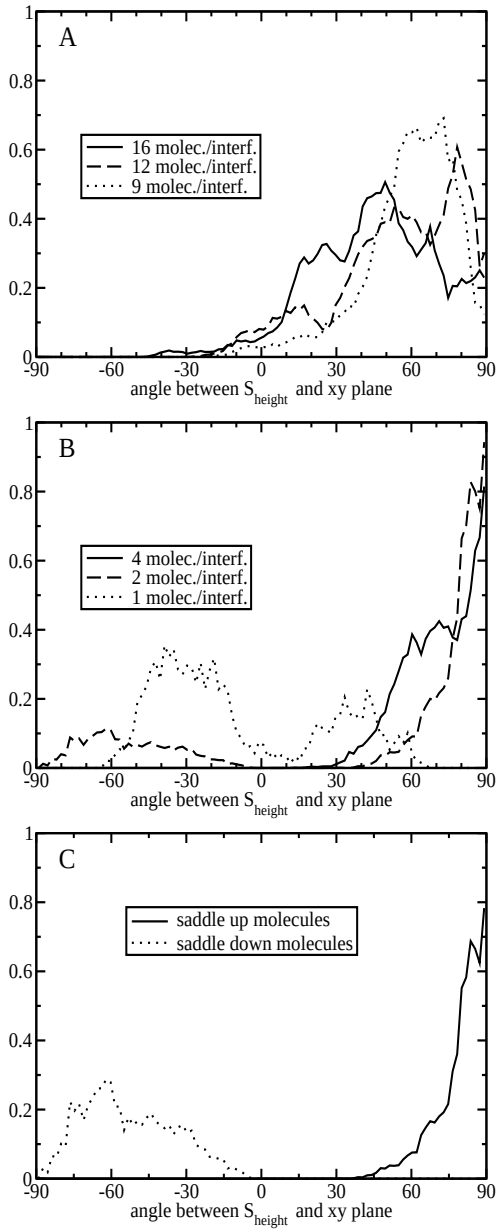


Figure 4.7: *Normalized distributions of the $\vec{S}_{height}$ angle at various interfacial concentrations. (*A*) 9, 12, and 16 surfactins per interface, (*B*) 4, 2, and 1 surfactins per interface and (*C*) at a concentration of 2 surfactins per interface plotted with contributions from tumbled over molecules (dotted line) or not (straight line).*

The tumbling of molecules is a surprising result as compared to previous models proposed from the molecular structure and experiments suggesting that hydrophilic amino-acids were oriented towards the hydrophilic part and the hydrophobic part was pointing to the hydrophobic medium or laying at the interface [77,78,87]. First, our results cannot be compared with a previous computed simulation study of surfactin conformation [93] where the interface was defined by the position of the hydrophilic and hydrophobic barycentres in a medium of intermediate dielectric constant. Furthermore, at low interfacial concentrations, lateral chains from the two hydrophilic residues of tumbled over molecules point into the core of the peptide avoiding interactions with the hydrophobic oil interface. This phenomenon has been ascertained by the orientation of the lateral chains (not shown) and the existence of hydrogen bonds as shown subsequently. Moreover, the low flexibility of tumbled molecules supports this model of a compact structure.

The global orientation of the molecule given by $\vec{S}_{height}$ orientation can be explained in terms of the orientation of the two vectors $\vec{S}_{top}$ and $\vec{S}_{base}$ placed at the base and the top of the tetrahedral model. At low concentrations, figure 4.8 *B* (left) shows a broad distribution centred on a mean value of 15 degrees for the $\vec{S}_{base}$ angle with a contribution in the range of 30-60 degrees for tumbled over molecules, while at higher concentrations *A* (left) the distribution is broader. At low concentration, the hydrophobic interface is a plane while at higher concentrations molecules are packed and thus create a hydrophobic environment for their neighbours. In figure 4.8 (right) we show fluctuations of the $\vec{S}_{top}$ vector orientation. The angle distribution is drifting towards low angle values as the interfacial concentration is decreasing. At high concentrations, the angle is about 50 degrees. This behaviour confirms the influence of the aggregation on the orientation of the molecules.

### Internal dimensions of the tetrahedral structure

The magnitudes of the three vectors $\vec{S}_{top}$, $\vec{S}_{base}$, and $\vec{S}_{height}$ give a complementary insight into the geometry of the surfactin molecule. The $\vec{S}_{height}$ vector magnitude varies from 2.9 to 4.9 Å as the secondary structure fluctuates (details not shown). Figure 4.9 shows the $\vec{S}_{base}$ and $\vec{S}_{top}$ magnitude distributions *versus* the surfactin concentration. Above four molecules per interface, the magnitude is about 5.6 Å, and 4.1 Å for the $\vec{S}_{base}$ and $\vec{S}_{top}$ vectors, respectively. At low concentrations, the $\vec{S}_{base}$ magnitude distribution is broad with a mean value of 6.5 Å, and the $\vec{S}_{top}$ magnitude distribution shows a broad peak around 6 Å and a sharper one around 4.1 Å, almost separated. At the lowest concentrations, where one molecule is upside down

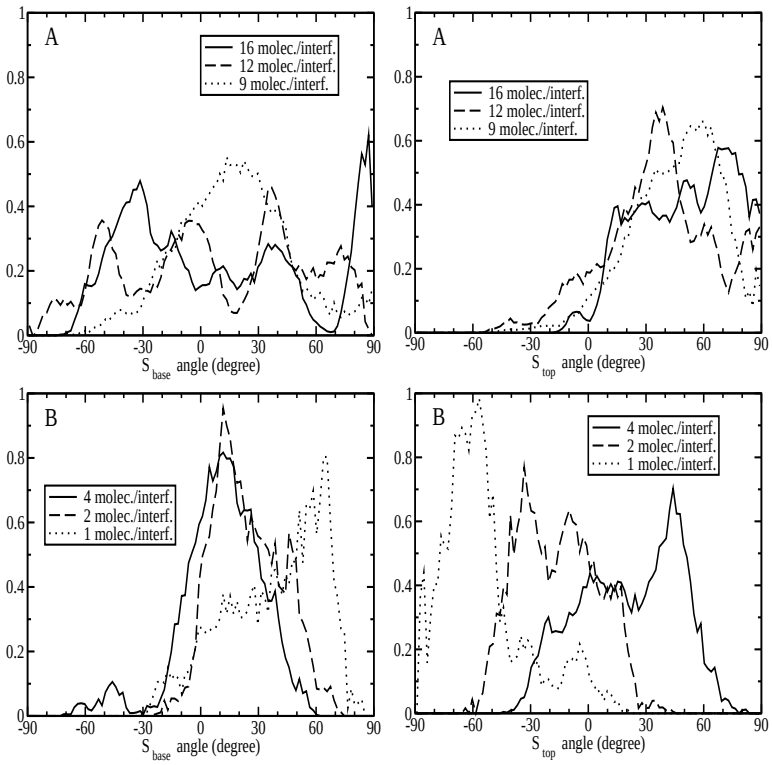


Figure 4.8: *Normalized distributions of the angle between $\vec{S}_{base}$ (left), $\vec{S}_{top}$ (right), and the* xy *plane parallel to the interface. (*A*) 9, 12, and 16 surfactins per interface, and (*B*) 4, 2, and 1 surfactins per interface.*

and the other one is tumbling, only the sharp peak is present in figure 4.9 *B* (right). In conclusion, concerning the free molecules, the hydrophilic peptidic part is compact when the molecule is tumbled over and its opposite side has an opened conformation. In this case, the $\vec{S}_{base}$ magnitude distribution reported on figure 4.9 *B* (left) has only one broad component due to the lactone part. This has a large ability to fluctuate compared to an amino acid residue. At the intermediate concentration of 4 molecules per interface, both distributions have a second component. The separation between the two components in figure 4.9 *B* (right) demonstrates the existence of two distinguishable conformational states of the hydrophilic side, "opened" or "closed". Clustered molecules surrounded by two neighbours are in a "closed" conformation while the others, in contact with less than one neighbour, are in an "opened" state. Two phenomena can explain this observation. The tran-

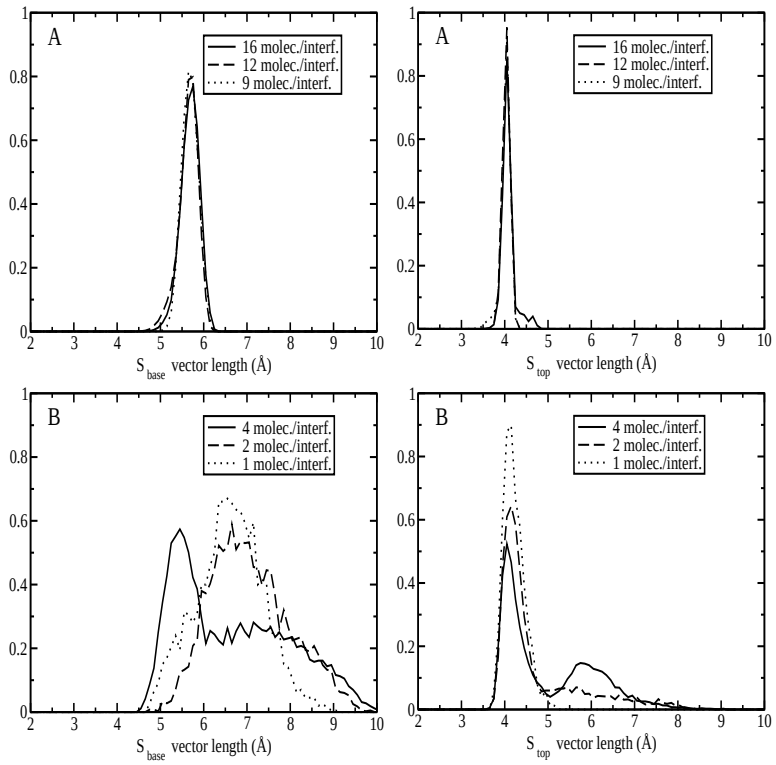


Figure 4.9: *Normalized distributions of the $\vec{S}_{base}$ (right) and $\vec{S}_{top}$ (left) vector magnitude at various concentrations. (*A*) 9, 12, and 16 surfactins per interface, and (*B*) 4, 2, and 1 surfactins per interface.*

sition from one state to the other obeys internal constraints and needs a significant activation energy, or the first transition state during the molecular opening adopts a geometry dependent on the first inserted molecule (as a water molecule in our case). However, the "closed" state of the hydrophilic side is observed in two cases, at a concentration of 4 surfactins per interface when molecules are clustered, and at lower concentrations when molecules are upside down. These occurrences suggest strongly that the "closed" conformation of the hydrophilic side is stabilized by internal hydrogen bonds favoured when interactions of the hydrophilic part with the aqueous phase are concealed or hindered by the environment by tumbling or packing of the peptidic part, respectively.

### Ramachandran angles

To complete the structure analysis and estimate the flexibility of surfactin molecules, we have recorded fluctuations of Ramachandran angles. At concentrations below 12 molecules per interface, upside down molecules have stable Ramachandran angles for all the residues except the terminal ones which are sensitive to the motions of the aliphatic tail and the lactone group. Moreover, those molecules exhibit the Ramachandran angles characteristic of a type II' $\beta$-turn Asp(5)→Leu(2). At a concentration of 2 and 4 molecules per interface, the free molecules and those clustered with only one neighbour are rather flexible and do not contain a particular structural motif. At a concentration of 9 surfactins per interface, about one third of the molecules are unstable when we consider the Ramachandran angles. They correspond to the molecules which are not yet part of a homogeneous surfactant monolayer.

At a concentration of 12 surfactins per interface, four molecules in total have few unstable angles corresponding to a *D*-Leu(3)-Val(4) peptide-plane flip with a ($\phi_4$; $\psi_3$) transition from (-90; -100) to (70; 100), the former state corresponding to the type II' $\beta$-turn and the latter one being metastable. This kind of peptide-plane flip is in agreement with previous work on peptide-plane motions [99], although it does not correspond to a transition between two stable conformations. With the exception of one molecule containing a *cis* *D*-Leu(3)-Val(4) conformation, all the other molecules have a type II' $\beta$-turn conformation.

At the highest concentration, one third of the molecules have unstable Ramachandran angles. Of the remaining two thirds, three molecules exhibit a peptide-plane flip as described above and four molecules adopt a non-conventional turn with (72±12; -100.5±5.7) and (-137±7; 40.25±9.1) as ($\phi_3$; $\psi_3$) and ($\phi_4$; $\psi_4$), respectively, which does not fall into allowed regions of the Ramachandran plot specific to each residue [100]. The remaining molecules contain a type II' $\beta$-turn. This unexpected conformation found at this concentration may result from the large lateral pressure applied on the surfactin molecules, inducing a conformational transition.

Angular fluctuations may explain the "chimeric" character of the molecule [90] observed experimentally. Motions of the peptidic backbone, as the coexistence of different conformers under identical physical conditions, induce a large distribution of the amide and the carboxylic groups orientation, yielding different absorption spectroscopic characteristics. But despite this angular variability, all the molecules at concentrations greater than 4 molecules per interface, have a similar hydrogen bond network.

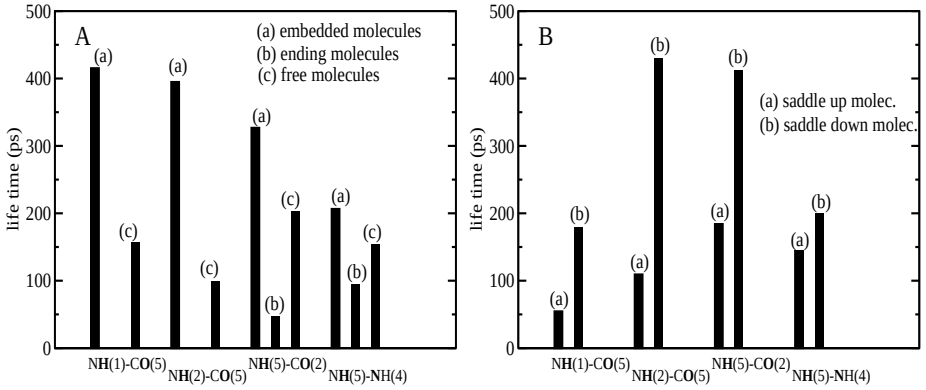


Figure 4.10: *Most frequent hydrogen bonds. (*A*) at high concentration for fully clustered molecules surrounded by more than one neighbour molecule (a), partially clustered molecules in contact with only one neighbour (b), and free molecules (c), and (*B*) at mean concentration for saddle up (a) and saddle down (b) molecules.*

### Intramolecular hydrogen bonds

In figures 4.10 *A* and *B* we illustrate the contributions of the most frequent intramolecular hydrogen bonds observed, excluding hydrogen bonds within carboxylic functions, at concentrations of 4 and 2 surfactins per interface, respectively.

Three hydrogen bonds have an occurrence probability longer than half of the simulated time. They are two "weak" bifurcated hydrogen bonds, NH(1)-CO(5) and NH(2)-CO(5), and the hydrogen bond characteristic of the conformer S1, NH(5)-CO(2). Those bonds mainly occur within packed molecules and upside down ones. It is worth noticing that those bonds, as defined by the method outlined above, are also detected from the coordinate set of conformer S1.

When focusing on less frequent hydrogen bonds, we notice that the Glu(1) carboxylic group is more often involved in intramolecular hydrogen bonds than the Asp(5) carboxylic group. This can be explained by the length of the Glu(1) lateral chain being larger than its analogue in the Asp(5) residue, allowing a greater flexibility. The oxygen atoms from Glu(1) interact preferentially with NH(7) and NH(1) while the rare bonds involving Asp(5) concern NH(5). Most of the molecules which are upside down have a hydrogen bond between Glu(1) and CO(7) too. Such interactions confirm the insertion of the carboxylic group in the peptide core when its residue is shielded from the

hydrophilic medium. Finally, most of the molecules which are not stabilized by the three most abundant hydrogen bonds present various hydrogen bonds such as NH(5)-NH(4), NH(3)-NH(2), NH(2)-NH(1) and NH(3)-CO(1) with various occurrence probabilities (from 10 to 30%).

At concentrations of 9, 12 and 16 surfactins per interface, the two hydrogen bonds NH(2)-CO(5), and NH(5)-CO(2) have an occurrence probability almost equal to the recorded time as NH(7)-COOH(1). Thus, albeit few molecules have conformational transitions as illustrated by their Ramachandran angle analysis, the type II' $\beta$-turn hydrogen bonds are preserved. Moreover, we observe few other hydrogen bonds rather stable as NH(5)-NH(4), NH(1)-CO(5), and COOH(1)-CO(7).

Whatever the concentration, we have never noticed hydrogen bonds between the two different carboxylic groups of a single molecule. Moreover, we have detected none of the three hydrogen bonds characteristic of the S2 conformer, NH(7)-CO(5), NH(4)-CO(2) and NH(6)-$C^1O$. This suggests that no transition is allowed from S1 conformer to S2 conformation under the physical conditions used for our simulations. On the other hand, we have also performed simulations starting from the S2 conformer. The characteristic structural parameters of this conformation which contains two $\gamma$-turns have not been conserved during the equilibration period. This confirms the S1 conformer as the most stable conformation at a hydrophilic/hydrophobic interface at a wide range of interfacial concentrations.

### 4.3.3 Interactions between a surfactin and its environment

The peptide is not big enough to have buried hydrogen acceptors or donors and only a few nitrogen and oxygen atoms were part of intramolecular hydrogen bonds. This suggests clearly that most of the remaining oxygen and nitrogen atoms interact with the solvent or other surfactins as hydrogen bond donor or acceptor.

In fact, very few hydrogen bonds between surfactin molecules have been detected. During the simulation, bonds involving the Asp(5) carboxylic group, and CO(1) and CO(2) groups, between two aggregated molecules at an interface, and the Glu(1) carboxylic group, and CO(6) and O(lactone) groups, between two other associated molecules at the other interface, have been identified at the highest surfactin concentration. However, these binding associations have rather different occurrence probabilities, 3.5% and 32.2%, respectively.

Hydrogen bonds between surfactin and water molecules are numerous. We have investigated hydrogen bonds involving a water molecule and two

residues and classified them as type I, II, or III depending on the geometry of the interaction between the water molecule (Hw-Ow-Hw) and the hydrogen bond donor (D) and acceptor (A), D-(Ow)-D, D-(Ow-Hw)-A, A-(Hw-Ow-Hw)-A, respectively. We assume that the donors and acceptors which are not involved in one of the previously described intra- and intermolecular hydrogen bonds interact with a single water molecule as D-Ow, A-Hw.

Most of the intermolecular hydrogen bonds have a probability smaller than 5%. But when we focus on the most stable bonds, we notice that hydrogen bonds of the type I are encountered between two consecutive amino acids NH(n)-NH(n+1) in the less compact surfactin molecules. Their occurrence probabilities are in the range of 30-60 %. Hydrogen bonds from type II are the most abundant except for molecules which are upside down. In this case, one of the most stable hydrogen bonds is linking the Glu(1) carboxylic group and CO(7). This bond can have a probability up to 100%. The less compact molecules are stabilized by a large number of hydrogen bonds of this type. The most specific bonds are between NH(1) or NH(2) and CO(5). Their occurrence probabilities are in a range of 10-100 %. Their presence is closely related to the increase of the "top" vector magnitude. As a consequence, compact molecules rarely have hydrogen bonds of type II and none of them seems to be stable within this molecular geometry. The last type of hydrogen bond, type III, is rather abundant. In packed molecules, bonds between CO(4)-CO(6) and CO(3)-$C_1O$ have a probability of 75 and 60%, respectively, while this value decreases dramatically for the other molecules, except for molecules which are upside down, where CO(3)-$C_1O$ is more abundant than CO(4)-CO(6).

In conclusion type I and III hydrogen bonds are mainly linking the peptide with its solvation shell, while type II bonds are characteristic of "opened" conformations of the hydrophilic moiety and take place between residues involved in the intramolecular hydrogen bonds present in packed molecules.

### 4.3.4 Interfacial properties

#### Diffusion coefficients

Rotational diffusion coefficient calculations are based on the motions of the $\vec{S}_{height}$ vector towards the interfacial plane while translational diffusion coefficients are computed from centres of mass displacements. An average of a vector ensemble motions should give a better description of the rotational behaviour. However, this vector is defined from the $\vec{S}_{base}$ and $\vec{S}_{top}$ vectors, thus local fluctuations are by definition partially averaged.

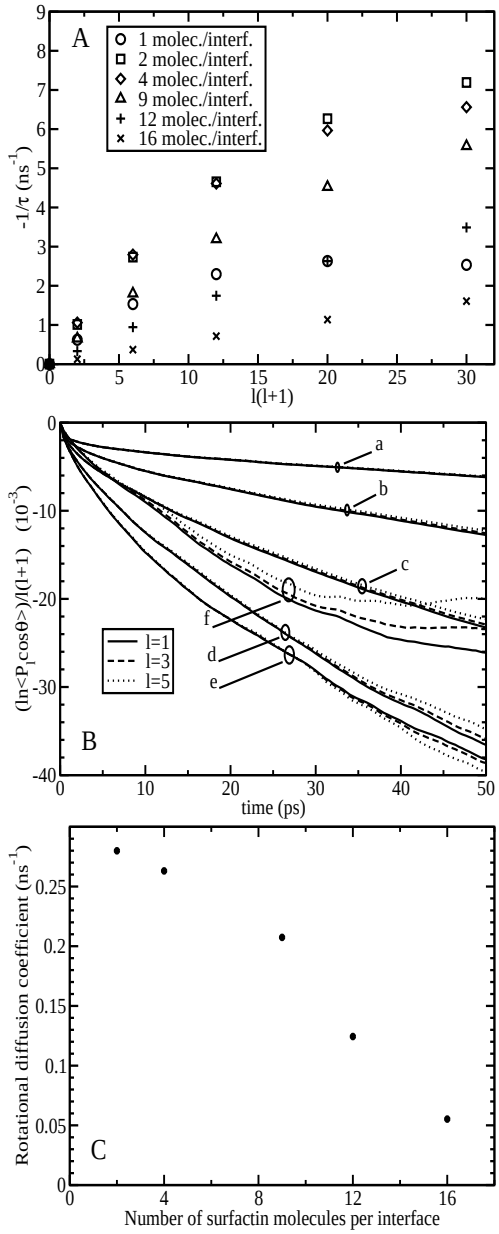


Figure 4.11: *(*A*) Inverse of the rotational relaxation time $\tau_l$ as a function of $l(l+1)$ corresponding to the five first Legendre polynomia $P_l$. (*B*) $ln\,\langle P_l[cos\theta(t)]\rangle$ as a function of time for three Legendre polynomia, $P_1$, $P_3$, and $P_5$, at 16 (a), 12 (b), 9 (c), 4 (d), 2 (e), and 1 (f) surfactins per interface.*

In figure 4.11 *A* $1/\tau_l$ is plotted *versus* $l(l+1)$ for all the concentrations. We observe a linear relationship for all concentrations except the lowest density one. This result validates the Debye model to describe the rotational motion despite the insertion of the aliphatic tail and the lateral chains from apolar residues in the hydrophobic medium. This likely tail perturbation might be averaged over all the molecule by interactions between amino acid lateral chains and solvents. Concerning the lowest concentration, two phenomena may explain this nonlinear behaviour. On the one hand, only two molecules contribute to the value, consequently, the statistical accuracy and validity of the results are quite low. Moreover, one of the two molecules has a fast tumbling over motion which brings a "non conventional" contribution to the global rotational motion studied. In figure 4.11 *B*, three logarithms of Legendre polynomial correlation functions are displayed. The short-time part of the curves contains some additional structure which could be related to internal motions of the protein and to rattling of the peptidic moiety within the solvent shell. The variation of the rotational diffusion coefficient with the interfacial concentration is plotted on figure 4.11 *C*.

Table 4.1 contains numerical values of both rotational and lateral diffusion coefficients. The rotational diffusion coefficient decreases as the interfacial concentration increases due to the lack of freedom for molecules at high interfacial concentrations. The lateral diffusion coefficient shows a dependence on the concentration from a concentration of 2-4 molecules per interface. At the lower concentration, our results present a poor statistical value. Moreover, the peptidic part of one of the two molecules has tumbled over on itself during the simulation. This rare motion may have affected the averaged value of the lateral diffusion coefficient.

### Interfacial tension and tangential pressure profile

Our studies on alkane liquid-vapour systems (chapter 2), hexane-water (chapter 3), and nonane/nonanol/water systems (not shown) show that the interfacial tension is correctly estimated for a large range of temperatures and surfactant concentrations, and differs less than $\sim$ 10% from experimental results, with the appropriate force field.

Simulated interfacial tensions are reported in table 4.1. Up to 9 molecules per interface, the interfacial tension is nearly constant. Above this limit, the interfacial tension can decrease dramatically until a minimal value of half the interfacial tension of a pure hexane/water system. This large decline in the interfacial tension illustrates the high interfacial activity of the surfactin molecule and gives an estimation of the "active" range of surfactin interfacial

| Interfacial concentration (molec./interface) | $D_T$ ($10^{-12}m^2.s^{-1}$) | $D_R$ ($ns^{-1}$) | $\gamma$ ($mN.m^{-1}$) |
|---|---|---|---|
| 0* | - | - | 46.0±1.6 |
| 1 | 670±120 | - | 47.4±1.7 |
| 2 | 950±220 | 0.280 | 44.3±1.6 |
| 4 | 320±140 | 0.263 | 49.7±1.7 |
| 9 | 260±140 | 0.207 | 46.2±1.9 |
| 12 | 230±70 | 0.124 | 31±2 |
| 16 | 180±60 | 0.055 | 18±2 |

Table 4.1: *Interfacial tension, rotational and lateral diffusion coefficients as a function of the number of surfactant per interface. * results from previous simulations concerning hexane-water binary system (see chapter 3).*

concentrations. The efficiency of surfactin in lowering the interfacial tension of a hexane-water system is comparable to its ability to reduce the water-air interfacial tension [77, 78].

Through the plot of the tangential component of the pressure profile, shown on figure 4.12, we can analyse the effect of surfactin molecules at the interface. At low concentrations, up to 4 molecules per interface, pressure profiles show a single structured peak. This peak contains contributions from a sharp peak characteristic of the oil/water interface, and a broader one related to the surfactin layer. While the concentration is increasing, direct contacts between oil and water phases are reduced by the surfactant film. At a concentration of 9 surfactin molecules per interface, the interface is fully covered by the surfactant layer and the lateral pressure profile contains several peaks. While the concentration is increasing, the profile is broader as the interfacial region is becoming thicker with an increasing number of surfactin molecules slightly popping out of the surfactant layer.

The reduction of the interfacial tension at concentrations higher than 9 surfactin molecules per interface (corresponding roughly to the interfacial concentration needed for a total covering of the oil/water interface) results mainly from the contribution of interactions between surfactant molecules which are not fully embedded in the surfactant layer and water or oil phase. They yield a positive contribution to the tangential pressure profile (considering that in the bulk phases, either the oil or water one, the tangential pressure profile is on average null).

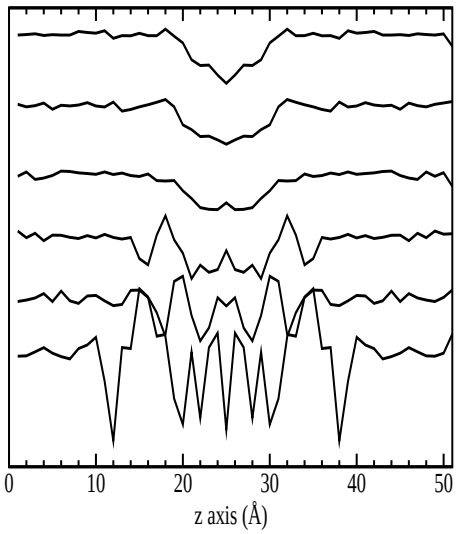


Figure 4.12: *Tangential pressure profiles at various concentrations. The oil interface is located at $z \approx 25$ Å, with the oil phase on the right side of the graph, and the aqueous one on the left side. This plot is an average of the tangential component of the pressure profile of the two interfaces and over a simulation of 0.5 ns for the different interfacial concentrations: 16, 12, 9, 4, 2, and 1 surfactin(s) per interface, from the bottom to the top, respectively.*

## 4.4 Concluding remarks

These simulations are the first molecular dynamics studies at an atomic level of surfactin in a liquid hydrophilic/hydrophobic interphase. They bring an interesting insight into the structural variability of the surfactin molecule depending on interfacial concentration and the molecular environment, and investigate the interfacial properties of this remarkable molecule. Since very few structure-activity correlation studies at a hydrophilic/hydrophobic interface have been carried out experimentally it is difficult to compare our results with existing data. However, the spectroscopic studies done in a homogeneous medium suggest a structural variability depending on the nature of the solvent and concentration of cations. In our model, which reproduces the native environment of the protonated form of surfactin, besides its salt concentration, we demonstrate that the conformation depends also on the environment of the molecule. Structural variability has already been observed [101, 102] when a peptidic segment was placed in a different medium. In this study,

we have demonstrated that placed at the same hydrophilic/hydrophobic interface, the surfactin molecule adopts different conformations depending on its interfacial concentration. Placed in a crowded environment, molecules are associated such that the interactions between hydrophobic residues and the hydrophilic medium are minimized. Such clusters are mainly stabilized by van der Waals interactions and from time to time by intermolecular hydrogen bonds involving carboxylic groups from side chains. Moreover, when hydrophilic residues are shielded from the environment, a complete tumbling over of the peptidic part can occur. This can be related to the ability of a surfactin molecule to pass through a hydrophobic medium as a lipid membrane. We hope that our description of the structural variability at this hydrophobic/hydrophilic interface will bring helpful insights for the interpretation of spectroscopic results.

From these results, we can assume that other environmental factors such as an organized and charged environment (as a zwiterionic lipid bilayer) will strongly affect the conformation of the surfactin molecule and its orientation as suggested by experimental results [85].

# Part C

# Biological membranes

# Chapter 5

# Tetraether lipid membranes.*

## 5.1 Introduction

Over the three domains of life, the "new" Archaeal [103] domain differs from the Eukarya and Bacteria by, for example, most of its genes [104]. Furthermore, Archaeal organisms are delimited by a single membrane mainly made of isoprenoid etherlipids [105] (instead of the abundant esterlipids found elsewhere, see for example [106]). The ability of archaeal organisms to live under extreme physical conditions, as high salt solutions, acid or alkaline medium, and low, or nearly water-boiling temperature ..., is directly related to the physical properties of the lipids of their membrane [107]. Archaeal membranes contain an isoprenoid hydrophobic core responsible for a low proton permeability which persists at high temperatures by an increase of the number of cyclopentane rings. The hydrophobic tails are linked to a glycerol group by an ether function, chemically more robust than an ester linkage.

*Thermoplasma acidophilum* is an archaeal organism with an optimal growth temperature of 55-59 °C and an optimal growth between pH 1 and 2 [108]. The lack of a cell wall supports the central role played by the membrane as a barrier against ion diffusion from low to high temperatures, maintaining physiological conditions (pH≈6) inside the cell while the organism lives in a strong acidic medium, i.e., a pH gradient of 5 pH units. The membrane of *Thermoplasma acidophilum* contains a rich variety of lipids, most of them (82%) being polar. The structure of the most abundant polar component, MPL (Main Polar Lipid, see Figure 5.1), has been recently identified [109]. It is a tetraether lipid with cyclopentane rings, and headgroups of phosphoglycerol and $\beta$-L-gulopyranose.

*based on: J.P. Nicolas and B. Smit. Molecular dynamics simulation of tetraether lipid membranes. *in preparation.*

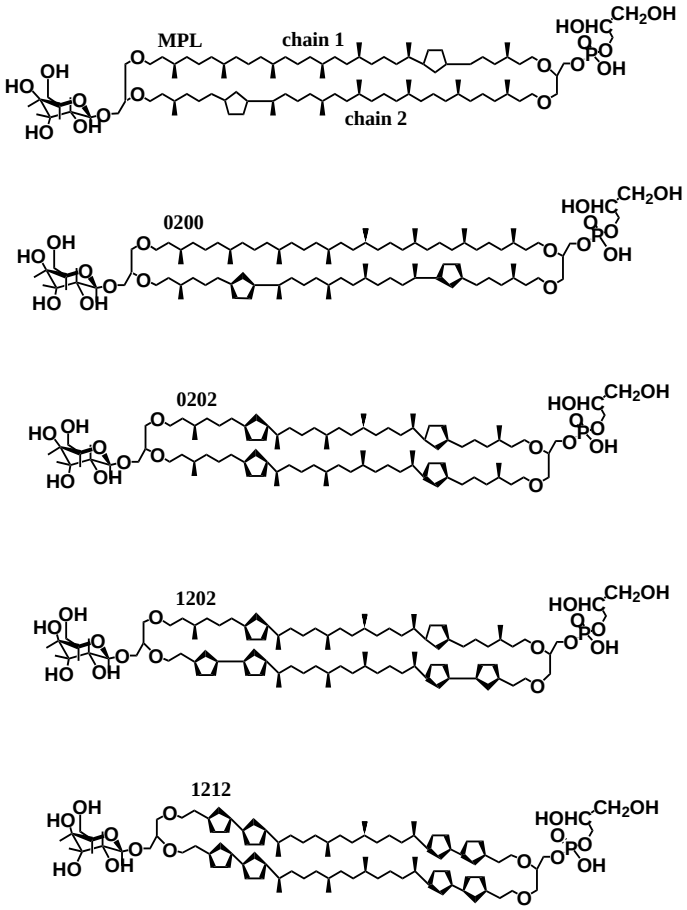


Figure 5.1: *Molecular structure of the Main Polar Lipid (top) from* Thermoplasma acidophilum*, and five analogues studied in this paper, from top to bottom: '0000', '0200', '0202', '1202', and '1212', where each digit gives the position of a ring, from one headgroup towards the mid-plane of the molecule, for the chain 2 and 1 successively. ("0" corresponds the absence of a ring, and only the two first positions along each half-chain are considered). On the gulose side, the cyclopentane rings are all* cis*, while on the phosphate side, they are either* trans*, or* cis*, or a mixture.*

Besides the work of Gabriel *et al.* [110] where for the first time different tetraether lipid membranes have been modelled, and the effect of cyclopentane rings on chain packing investigated, to the best of our knowledge, there has been no published molecular dynamics study of the structure and dynamics of tetraether lipid membranes. In this chapter, we study the structure of five membranes purely built from MPL analogues (see Figure 5.1). Furthermore, we investigate the influence of the cyclopentane rings and their stereochemistry on the membrane organization and the lateral pressure profile.

## 5.2 Molecular dynamics

Molecular dynamics computer simulations were carried out using the DL-POLY package [59]. An all-atom model was employed to describe molecules at an atomic scale using the potential energy parameter set PARM27 from the CHARMM package [55]. The TIP3P water model [56] was used in all simulations. Bonds involving hydrogen were held fixed with the SHAKE algorithm [18]. Electrostatic interactions were computed using the Smooth Particle Mesh Ewald method [57]. Our simulations were performed in the NVT ensemble [60], i.e., with constant temperature, volume, and number of particles. Simulations were run with periodic boundary conditions. All the simulations were performed using a cutoff radius of 12 Å for the van der Waals terms.

For each of the five lipids, we have used the same protocol to build up the corresponding hydrated membrane model. Initially, a single lipid molecule stretched along its longer axis was pre-equilibrated in vacuum. After, we have built our complete models by placing the lipids on a $6 \times 6$ grid, with carbohydrate headgroups forming one outer side of the membrane, and phosphate headgroups the other interface, mimicking the asymmetrical topology found *in vivo* [111, 112], both membrane surfaces being parallel to the $xy$ plane. The size of the grid is set such as to get a positive lateral pressure within the membrane, and the length of the simulation box along the $z$ axis such that the two membrane interfaces do not interact. The dry membrane has been equilibrated during a few hundred steps coupled to a gradual increase of the time step until 2 fs. Subsequently, the box is filled by adding water molecules. In such a way that the system contains 36 lipid molecules, and more than 2.200 water molecules, thus approximatively 17.000 atoms, and 30 water molecules per lipid headgroup, which corresponds to a fully hydrated membrane. The molecular area per lipid is 59.27, 58.57, 60, 62, and 62.73

Å$^2$, for the '0000', '0202', '0200', '1202', and '1212' MPL lipid analogues, respectively.

The complete system has been equilibrated for 250.000 steps, with a time step of 2 fs at a temperature of 300 K. During equilibration, density profiles and energy convergence of the system have been monitored. After equilibration, we have recorded the dynamics of the system by accumulating coordinates at an interval of 0.1 ps during a period of 0.8 ns. An extension with 1.6 ns of molecular simulation has been achieved to get an accurate lateral pressure profile.

## 5.3 Results and discussion

### 5.3.1 Mass and electronic density profiles

Figure 5.2 reports the mass density profile and its components for the five membranes, and the electronic density profile of the '1212' lipid membrane. From the total mass and electronic density profiles of the '1212' lipid membrane, which is the model membrane which contains the larger number of cyclopentane rings, we observe two high and sharp peaks, each located at the headgroup-water interface. They correspond to the sum of the contributions of the glycerol group, and the phosphate or gulose moiety.

From the '1212' model to the '0000' model, the decrease of the number of cyclopentane rings yields a broadening and a diminishing of the headgroup density peaks. This is associated with a reduction of the ordering of the aliphatic chains. The overlap between density profile components is rather important in the '0000' membrane model, while almost nonexistent in the '1212' membrane model profile. The cyclopentane rings are responsible for a higher ordering of both the membrane core and each interface. The width of the aliphatic domain is reduced as the number of cyclopentane rings increases, as noticed from the first energy minimization study of a similar kind of membranes [110].

For all the model membranes, the shape of the electronic (only the '1212' model is shown) and mass density profile is nearly identical. Both density profiles show small features in the membrane phase, which suggest, considering the long recording time of the density profiles (0.8 ns), that the membranes are in a phase where motions are rather slow, as a "gel" phase (a fluid phase would have given a density profile with a smooth and almost flat density profile in the hydrophobic region). This observation does not depend on the degree of cyclization of the aliphatic chains and is consistent with previous results from molecular modelling [110].

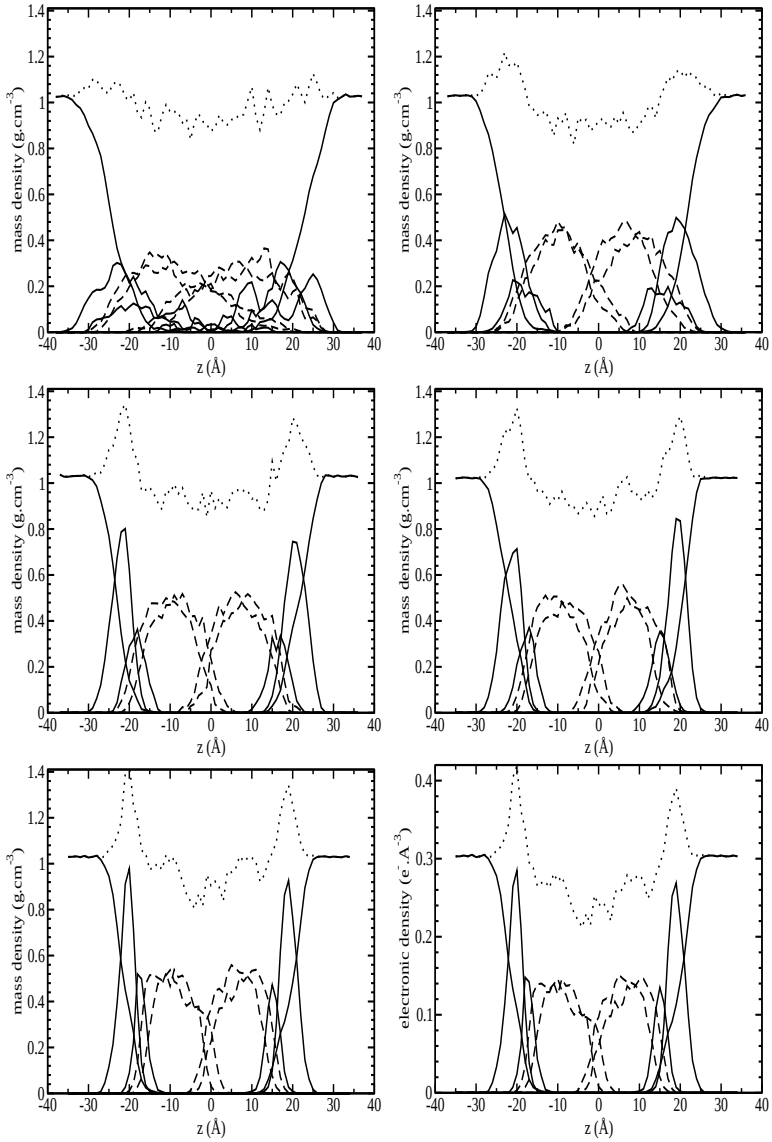


Figure 5.2: *Mass density profiles of the '0000' (top left), '0200' (top right), '0202' (centre left), '1202' (centre right), and '1212' (bottom left) lipid membranes. Electronic density profile of '1212' (bottom right) lipid membrane. The gulose is on the right interface, while the phosphate group is on the left one. The total density profile is represented by the dotted curve. From the centre of the membrane ($z \approx 0$ Å) to the right, are reported one half of the chain 1 and one half of the chain 2 (on the saccharide side) (dashed curves), the glycerol linked to the gulose group and water (solid curves). From the centre of the membrane to the left, are reported one half of the chain 1 and one half of the chain 2 (on the phosphate side) (dashed curves), the glycerol linked to the phosphate group and water (solid curves).*

Furthermore, while the aliphatic chains are identical in their connectivities on both sides of the membrane mid-plane, the density profiles show a slight asymmetry. Either the configurational isomerism of each aliphatic chain moiety (resulting from the different absolute configuration of the carbon stereocentres involved in cyclopentane rings) induces a peculiar molecular conformation which yields specific density profile features, or the two sides of the membrane simulated in the gel phase have been trapped in different conformations. These hypotheses will be discussed later in this chapter.

### 5.3.2 Molecular orientation

The orientation of parts of the lipid molecules, as the aliphatic chains or the headgroups, can be described by an order parameter. In the case of the aliphatic chains, we have defined two complementary parameters. First, we have computed the orientation of carbon chains from the vector defined by the coordinates of two carbons $n$ and $n+2$ belonging to the same chain. By skipping the carbon $n+1$, the computed orientation of a chain segment is given without the contribution of the peculiar zigzag conformation of an aliphatic chain. Moreover, we have computed the C–H vector orientation, which can directly be compared to the Scd chain parameter obtained from NMR spectroscopy. The order parameter reads:

$$S(z) = \frac{1}{2}\langle 3\cos^2\theta(z) - 1\rangle, \tag{5.1}$$

where $\theta$ is the angle between the vector C–C or C–H and the interface normal. A value close to 1 corresponds to a distribution of vectors parallel to the normal of the interface, while a distribution of vectors parallel to the membrane plane yields an order parameter close to $-0.5$. When the vector angles are randomly distributed, the order parameter will be equal to 0 (although an order parameter equal to 0 may also correspond to a phase perfectly ordered, with a tilt angle distribution centred on 54.7 degrees).

Figure 5.3 reports the C–C and C–H order parameters for each membrane. The numbering of atoms starts from the mid-plane of the molecule, and we assign to the vector the number/label of the carbon atom which defines the origin of the C–H vector, or the (skipped) $n+1$ carbon of the $(n)$–$(n+2)$ C–C vector. Only C–C vectors computed from the main carbon chain are shown. C–H vectors involved in cyclopentane rings are not reported.

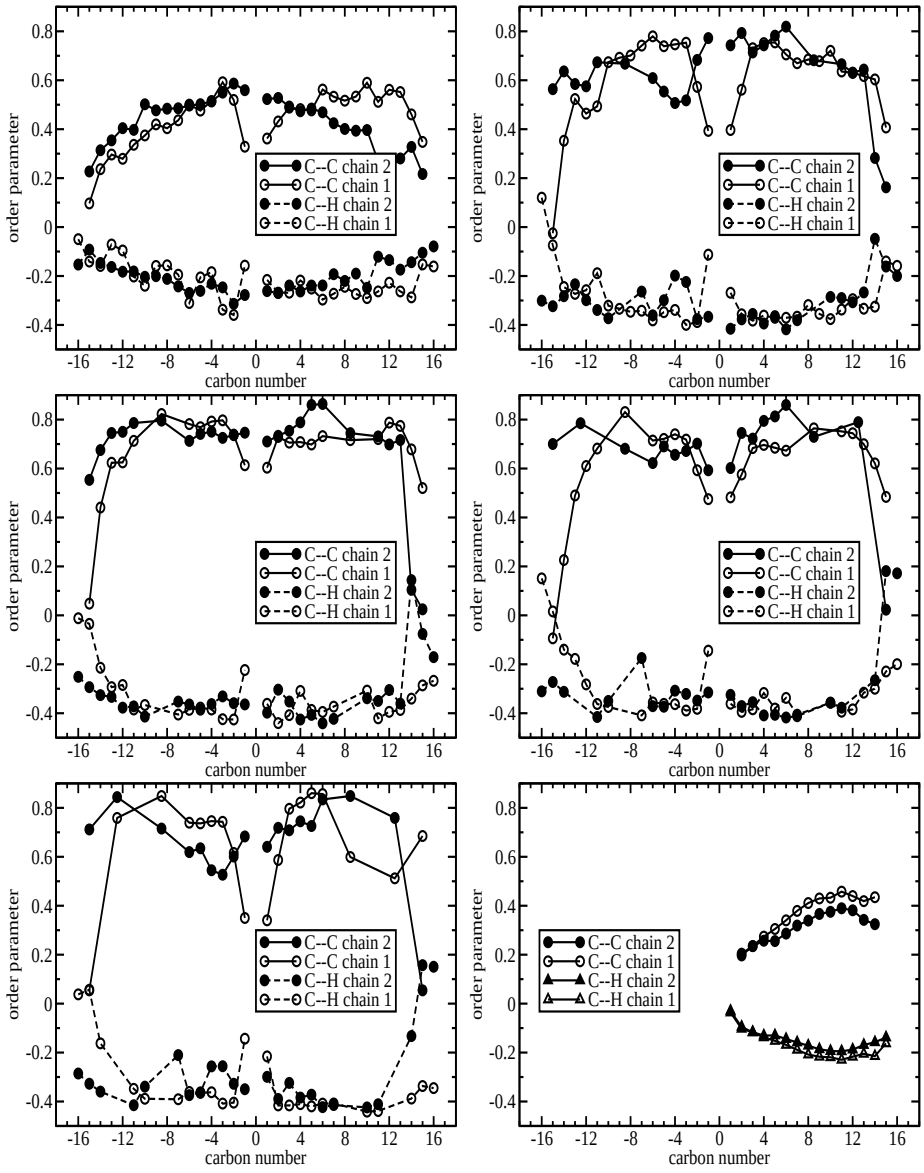


Figure 5.3: *Order parameter of the hydrophobic chains for each lipid membranes: '0000' (top left), '0200' (top right), '0202' (centre left), '1202' (centre right), and '1212' (bottom left). The gulose is on the right interface, while the phosphate group is on the left one. For comparison, the order parameter of a DPPC lipid molecule embedded in a membrane is reported too (bottom right).*

MPL lipid differs from the more classical DPPC (di-palmitoyl-phosphatidyl-choline) phospholipid by the spanning geometry of the lipid within the membrane, and the presence of methylene groups or cyclopentane rings on the aliphatic backbones, plus a few other features as the ether linkage. As we compare the two order parameters between a DPPC and a '0000' MPL membrane, we notice that the archaeal lipid membrane is on the whole much more ordered, with a maximum value of the order parameter located within the hydrophobic core of the membrane, close to the mid-plane of the membrane, while it is located on the headgroup side in the case of the DPPC membrane, and decreases slowly as the carbons get closer to the mid-plane. This major difference can be related to both the presence of methylene lateral groups, which act as spurs located on the chain backbone, and the transmembrane geometry of the backbone itself.

From Figure 5.4 which reports the angle distribution between the main axis of the aliphatic chains and the normal to the membrane plane, we cannot detect an effect of the number of rings. The orientation of the lipid molecules varies from 0 to 15 degrees. This is consistent with previous experimental results [112] obtained with bipolar lipid membranes at a water-water interface. Figure 5.3 shows an increase of the membrane order as soon as the lipid molecules contain one cyclopentane ring. However, the presence of additional rings does not improve the chain ordering. At the chain-ends, the aliphatic chain orientation is perturbed by the linkage to the glycerol, especially concerning the chain-end connected to the centre of the glycerol (via the ester linked to the central carbon of the glycerol). This suggests that small motions of both phosphate and gulose headgroups induce a slight disorder on the position of the outermost hydrophobic carbons.

The C–C bonds located at the hydrophobic mid-plane of the lipid molecules are in some cases less oriented compared to the other C–C bonds. This behaviour can be related to the length of the carbon chains which depends on both the number of cyclopentane rings per chain, and the conformation imposed by the stereochemistry of the carbons involved in the cyclopentane rings. Last, the C–C bond vector related to the cyclopentane rings (see the positions at $\pm 8.5$ and $\pm 12.5$ on the graphs) do not have a prefered orientation specific to a peculiar *cis* or *trans* ring substitution, but give an insight on the local conformation adopted by the rings.

Last, the cyclopentane rings, located in these membrane models on the two outest methylene group positions, improve the order of the chain, counterbalancing the effect of headgroup motions observed for the 0000 model. This is consistent with the thin shape of the headgroup component peak of

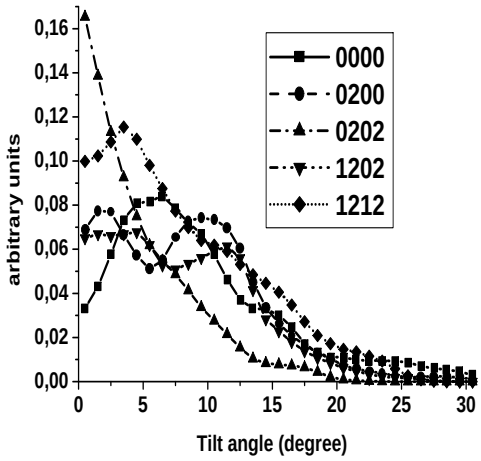


Figure 5.4: *Orientation of the aliphatic chains relative to the membrane plane normal.*

the density profiles, described above.

### 5.3.3 Pressure profiles

Figure 5.5 reports the pressure profile for the five kinds of membranes. As seen in the previous sections, when the number of cyclopentane rings increases, the ordering of the membrane both improves and differs from one side of the membrane to the other. We observe a similar trend in the pressure profiles. For the '0000' membrane model, the symmetry associated with a low ordering of the membrane yields a rather symetrical pressure profile. But as the number of rings increases, the pressure profile is different on each side of the membrane. This is especially noticeable for membranes made of lipids containing more than 4 rings. Since the high pressure profiles are always located on the same side of the membrane, characterized by a specific configuration, this peculiar pressure profile shape is related to the absolute configuration of the carbon stereocentres (and not to a trapped conformation).

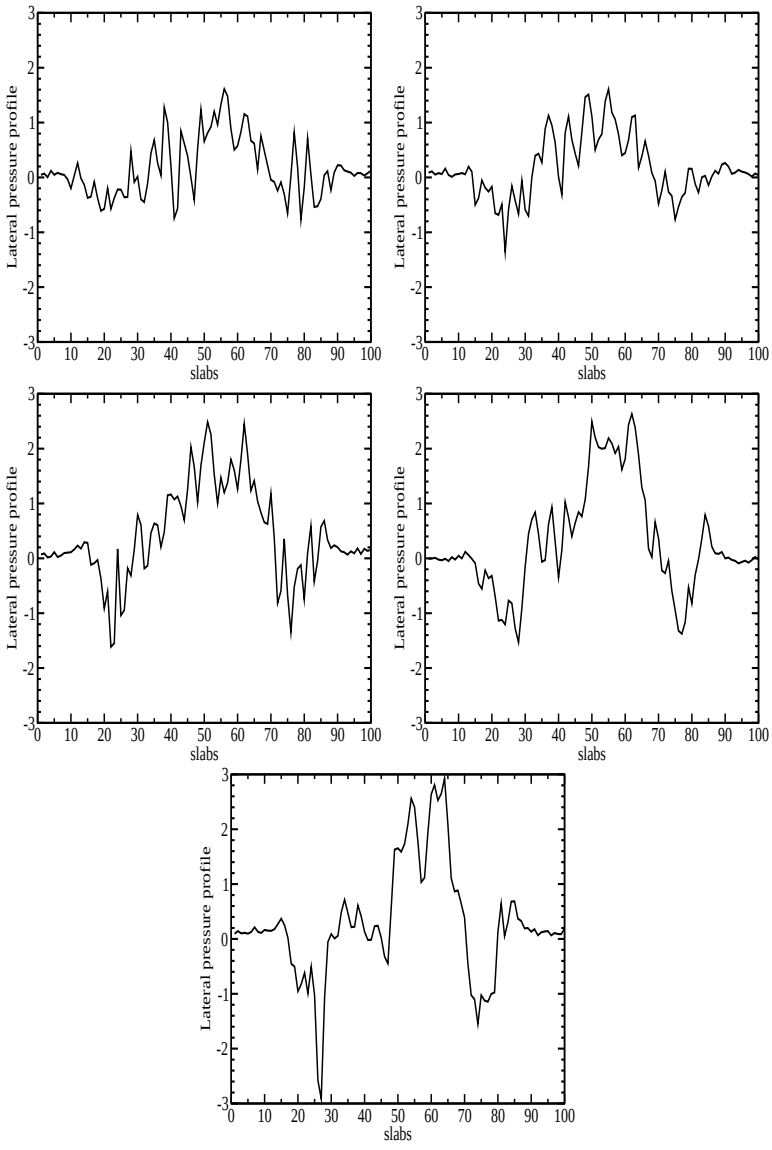


Figure 5.5: *Pressure profile of the '0000' (top left), '0200' (top right), '0202' (centre left), '1202' (centre right), '1212' (bottom) lipid membranes.*

The two interfacial headgroups are responsible for a negative or null contribution to the pressure profile. That means no stress is imposed by the two ends of the lipid. In addition, it is worth noticing that compared to phosphatidylcholine membranes, the pressure profile does not vanish in the mid-plane region, but only depends on the membrane conformation. This is a consequence of the spanning position of this peculiar kind of lipids.

## 5.4 Concluding remarks

The class of lipid, made of two spanning aliphatic chains linked to a phosphate and a sugar headgroup by two ether bonds and a glycerol group, presents properties dramatically different from the more familiar phospholipids. Chemically, they are much more stable, and form large and stable liposomes, being an ideal candidate as a drug delivery vector model for extreme media. Consequently, the synthesis of archaeal lipid analogues represents an interesting challenge for both a fundamental and an industrial point of view (see for example, [113–117]).

While the complete inventory of the lipid structures present in archaeal organisms is still in progress [105, 109, 118–120], being a difficult task mainly by the high variability of the sugar headgroups, very little information was available on the molecular shape and the membrane organization at an atomic scale [110, 121–129].

To our knowledge, this work is the first report of a significant molecular dynamics study done on tetraether membrane models using simulation techniques. The atomic description of the membrane model allows a detailed analysis of the membrane organization. Thus, as suggested by experimental results [130], the membrane organization is determinated by the hydrophobic core. We found from the analysis of the order parameters of the aliphatic chains that the cyclopentane rings increase the ordering of the membrane, which maintains the low permeability of the membrane when the temperature increases. But, the main finding of this work concerns the relation between the absolute configuration of stereocentres located on the aliphatic chains and the organization of the membrane in its hydrophobic domain.

Such peculiar properties of these lipids [107, 131], correlated to the high dependence of the pressure profile on the chain conformation, suggests this class of molecules as an ideal tool in the study of the relation between the membrane pressure profile and the regulation of an ion-channel protein complex.

# Bibliography


[1] J. C. Shelley and M. Y. Shelley. Computer simulation of surfactant solutions. *Curr. Opin. Colloid Interf. Sci.*, 5:101–110, 2000.

[2] M. P. Allen and D. J. Tildesley. *Computer Simulation of Liquids.* Clarendon Press, Oxford, 1989.

[3] D. Frenkel and B. Smit. *Understanding molecular simulation: From algorithms to applications.* Academic Press, San Diego, 2002.

[4] B. Smit, S. Karaborni, and J. I. Siepmann. Computer simulations of vapor-liquid phase equilibria of $n$-alkanes. *J. Chem. Phys.*, 102:2126–2140, 1995.

[5] M. Mondello and G. S. Grest. Molecular dynamics of linear and branched alkanes. *J. Chem. Phys.*, 103:7156–7165, 1995.

[6] M. G. Martin and J. I. Siepmann. Predicting multicomponent phase equilibria and free energies of transfer for alkanes by molecular simulation. *J. Am. Chem. Soc.*, 119:8921–8924, 1997.

[7] S. K. Nath, F. A. Escobedo, and J. J. De Pablo. On the simulation of vapor-liquid equilibria for alkanes. *J. Chem. Phys.*, 108:9905–9911, 1998.

[8] J. J. Potoff, J. R. Errington, and A. Z. Panagiotopoulos. Molecular simulation of phase equilibria for mixtures of polar and non-polar components. *Mol. Phys.*, 97:1073–1083, 1999.

[9] J. Delhommelle, A. Boutin, and A. H. Fuchs. Molecular simulation of vapor-liquid coexistence curves for hydrogen, sulfide-alkane and carbon dioxane-alkane mixtures. *Molec. Sim.*, 22:351–368, 1999.

[10] J. D. Moore, S. T. Cui, H. D. Cochran, and P. T. Cummings. Rheology of lubricant basestocks: a molecular dynamics study of $C_{30}$ isomers. *J. Chem. Phys.*, 113:8833–8840, 2000.

[11] C. McCabe, S. Cui, P. T. Cummings, P. A. Gordon, and R. B. Saeger. Examining the rheology of the 9-octylheptadecane to giga-pascal pressures. *J. Chem. Phys.*, 114:1887–1891, 2001.

[12] M. Mondello, G. S. Grest, E. B. Webb III, and P. Peczak. Dynamics of $n$-alkanes: comparison to Rouse model. *J. Chem. Phys.*, 109:798–805, 1998.

[13] W. L. Jorgensen, J. D. Madura, and C. J. Swenson. Optimized intermolecular potential functions for liquid hydrocarbons. *J. Am. Chem. Soc.*, 106:6638–6646, 1984.

[14] J. Alejandre, D. J. Tildesley, and G. A. Chapela. Fluid phase equilibria using molecular dynamics: the surface tension of chlorine and hexane. *Mol. Phys.*, 85:651–663, 1995.

[15] M. Laso, J. J. De Pablo, and U. W. Suter. Simulation of phase equilibria for chain molecules. *J. Chem. Phys.*, 97:2817–2819, 1992.

[16] J. J. De Pablo, M. Laso, J. I. Siepmann, and U. W. Suter. Continuum-configurational-bias Monte Carlo simulations of long-chain alkanes. *Mol. Phys.*, 80:55–63, 1993.

[17] J. P. Ryckaert and A. Bellemans. Molecular dynamics of a liquid $n$-butane near its boiling point. *Chem. Phys. Lett.*, 30:123–125, 1975.

[18] J. P. Ryckaert, G. Ciccotti, and H. J. C. Berendsen. Numerical integration of the cartesian equations of motion of a system with constraints: molecular dynamics of $n$-alkanes. *J. Comput. Phys.*, 23:327–341, 1977.

[19] P. Van Der Ploeg and H. J. C. Berendsen. Molecular dynamics simulation of a bilayer membrane. *J. Chem. Phys.*, 76:3271–3276, 1982.

[20] D. J. Evans and G. P. Morriss. Non-newtonian molecular dynamics. *Comp. Phys. Rep.*, 1:297–343, 1984.

[21] version 2.11. Dlpoly 2.11, 1999.

[22] J. J. Jasper, E. R. Kerr, and F. Gregorich. The orthobaric surface tensions and thermodynamic properties of the liquid surfaces of the $n$-alkanes, $C_5$ to $C_{28}$. *J. Am. Chem. Soc.*, 75:5252–5254, 1953.

[23] J. J. Jasper and E. V. Kring. The isobaric surface tensions and thermodynamic properties of the surfaces of a series of $n$-alkanes, $C_5$ to $C_{18}$, 1-alkens, $C_6$ to $C_{16}$, and of $n$-decylcyclopentane, $n$-decylcyclohexane, and $n$-decylbenzene. *J. Phys. Chem.*, 59:1019–1021, 1955.

[24] D. Fincham, N. Quirke, and D. J. Tildesley. Computer simulation of molecular liquid mixtures. I. A diatomic Lennard-Jones model mixture for $CO_2/C_2H_6$. *J. Chem. Phys.*, 84:4535–4546, 1986.

[25] B. D. Smith and R. Srivastava. *Thermodynamics Data for Pure Compounds: Part A Hydrocarbons and Ketones.* Elsevier, Amsterdam, 1986.

[26] B. Smit and D. Frenkel. Vapor-liquid equilibria of the two-dimensional Lennard-Jones fluid(s). *J. Chem. Phys.*, 94:5663–5668, 1991.

[27] B. Smit. Phase diagrams of Lennard-Jones fluids. *J. Chem. Phys.*, 96:8639–8640, 1992.

[28] B. Smit, S. Karaborni, and J. I. Siepmann. Erratum: "Computer simulations of vapor-liquid phase equilibria of $n$-alkanes" [J. Chem. Phys. 102, 2126 (1995)]. *J. Chem. Phys.*, 109:352, 1998.

[29] M. G. Martin and J. I. Siepmann. Transferable potentials for phase equilibria. I. United-atom description of $n$-alkanes. *J. Phys. Chem. B*, 102:2569–2577, 1998.

[30] J. P. R. B. Walton, D. J. Tildesley, J. S. Rowlinson, and J. R. Henderson. The pressure tensor at a planar surface of a liquid. *Mol. Phys.*, 48:1357–1368, 1983.

[31] J. G. Kirkwood and F. P. Buff. The statistical mechanical theory of surface tension. *J. Chem. Phys.*, 17:338–343, 1949.

[32] M. J. P. Nijmeijer, A. F. Bakker, C. Bruin, and J. H. Sikkenk. A molecular dynamics simulation of the Lennard-Jones liquid-vapor interface. *J. Chem. Phys.*, 89:3789–3792, 1988.

[33] J. S. Rowlinson. Thermodynamics of inhomogeneous systems. *Pure Appl. Chem.*, 65:873–882, 1993.

[34] J.S. Rowlinson and B. Widom. *Molecular Theory of Capillarity.* Clarendon Press, Oxford, 1982.

[35] I. Benjamin. Molecular structure and dynamics at liquid-liquid interfaces. *Annu. Rev. Phys. Chem.*, 48:407–451, 1997.

[36] J. Penfold. The structure of the surface of pure liquids. *Rep. Prog. Phys.*, 64:777–814, 2001.

[37] N. Morrow. *Interfacial phenomena in petroleum recovery.* Marcel Dekker Incorporation, New York, 1990.

[38] L. R. Pratt and A. Pohorille. Hydrophobic effects and modeling of biophysical aqueous solution interfaces. *Chem. Rev.*, 102:2671–2692, 2002.

[39] D. M. Huang and D. Chandler. The hydrophobic effect and the influence of solute-solvent attractions. *J. Phys. Chem. B*, 106:2047–2053, 2002.

[40] F. P. Buff, R. A. Lovett, and F. H. Stillinger Jr. Interfacial density profile for fluids in the critical region. *Phys. Rev. Letters*, 15:621–623, 1965.

[41] A. Braslau, M. Deutsch, P. S. Pershan, A. H. Weiss, J. Als-Nielsen, and J. Bohr. Surface roughness of water measured by X-ray reflectivity. *Phys. Rev. Letters*, 54:114–117, 1985.

[42] D. Beaglehole. Capillary-wave and intrinsic thicknesses of the surface of a simple liquid. *Phys. Rev. Letters*, 58:1434–1436, 1987.

[43] D. Beysens and J. Meunier. Comment on "Capillary-wave and intrinsic thicknesses of the surface of a simple liquid". *Phys. Rev. Letters*, 61:2002, 1988.

[44] A. Braslau, P. S. Pershan, G. Swislow, B. M. Ocko, and J. Als-Nielsen. Capillary waves on the surface of simple liquids measured by X-ray reflectivity. *Phys. Rev. A*, 38:2457–2470, 1988.

[45] D. K. Schwartz, M. L. Schlossman, E. H. Kawamoto, G. J. Kellogg, P. S. Pershan, and B. M. Ocko. Thermal diffuse x-ray-scattering studies of the water-vapor interface. *Phys. Rev. A*, 41:5687–5690, 1990.

[46] I. Benjamin. Theoretical study of the water/1,2-dichloroethane interface: Structure, dynamics, and conformational equilibria at the liquid-liquid interface. *J. Chem. Phys.*, 97:1432–1445, 1992.

[47] L. T. Lee, D. Langevin, E. K. Mann, and B. Farnoux. Neutron reflectivity at liquid interfaces. *Physica B*, 198:83–88, 1994.

[48] B. M. Ocko, X. Z. Wu, E. B. Sirota, S. K. Sinha, and M. Deutsch. X-ray reflectivity study of thermal capillary waves on liquid surfaces. *Phys. Rev. Letters*, 72:242–245, 1994.

[49] S. Dietrich. Structures in fluids induced by interfaces. *J. Phys.: Cond. Matter*, 8:9127–9141, 1996.

[50] J. C. Conboy, J. L. Dashbach, and G. L. Richmond. Total internal reflection second-harmonic generation: probing the alkane water interface. *Appl. Phys. A*, 59:623–629, 1994.

[51] A. Goebel and K. Lunkenheimer. Interfacial tension of the water/$n$-alkane interface. *Langmuir*, 13:369–372, 1997.

[52] D. E. Gragson and G. L. Richmond. Comparisons of the structure of water at neat oil/water and air/water interfaces as determined by vibrational sum frequency generation. *Langmuir*, 13:4804–4806, 1997.

[53] S. Zeppieri, J. Rodríguez, and A. L. López de Ramos. Interfacial tension of alkane + water systems. *J. Chem. Eng. Data*, 46:1086–1088, 2001.

[54] M. L. Schlossman. Liquid-liquid interfaces: studied by X-ray and neutron scattering. *Curr Opin. Coll. Interf. Sc.*, 7:235–243, 2002.

[55] A. D. MacKerell, Jr., D. Bashford, M. Bellott, R. L. Dunbrack, Jr., J. D. Evanseck, M. J. Field, S. Fischer, J. Gao, H. Guo, S. Ha, D. Joseph-McCarthy, L. Kuchnir, K. Kuczera, F. T. K. Lau, C. Mattos, S. Michnick, T. Ngo, D. T. Nguyen, B. Prodhom, W. E. Reiher, III, B. Roux, M. Schlenkrich, J. C. Smith, R. Stote, J. Straub, M. Watanabe, J. Wiórkiewicz-Kuczera, D. Yin, and M. Karplus. All-atom empirical potential for molecular modeling and dynamics studies of proteins. *J. Phys. Chem. B*, 102:3586–3616, 1998.

[56] W. L. Jorgensen, J. Chandrasekhar, J. D. Madura, R. W. Impey, and M. L. Klein. Comparison of simple potential functions for simulating liquid water. *J. Chem. Phys.*, 79:926–935, 1983.

[57] U. Essmann, L. Perera, M. L. Berkowitz, T. Darden, H. Lee, and L. G. Pedersen. A smooth particle mesh Ewald method. *J. Chem. Phys.*, 103:8577–8593, 1995.

[58] K. Binder and M. Müller. Computer simulation of profiles of interfaces between coexisting phases: do we understand their finite size effects? *Int. J. Modern Phys. C*, 11:1093–1113, 2000.

[59] version 2.12. Dlpoly 2.12, 2001.

[60] W. G. Hoover. Canonical dynamics: equilibrium phase-space distributions. *Phys. Rev. A*, 31:1695–1697, 1985.

[61] J. D. Weeks. Structure and thermodynamics of the liquid-vapor interface. *J. Chem. Phys.*, 67:3106–3121, 1977.

[62] S. W. Sides, G. S. Grest, and M. D. Lacasse. Capillary waves at liquid-vapor interfaces: a molecular dynamics simulation. *Phys. Rev. E*, 60:6708–6713, 1999.

[63] J. L. Rivera, C. McCabe, and P. T. Cummings. Molecular simulations of liquid-liquid interfacial properties: water–*n*-alkane and water-methanol–*n*-alkane systems. *Phys. Rev. E*, 67:011603, 2003.

[64] S. Senapati and M. L. Berkowitz. Computer simulation study of the interface width of the liquid/liquid interface. *Phys. Rev. Letters*, 87:176101, 2001.

[65] J. P. Nicolas and B. Smit. Molecular dynamics simulations of the surface tension of *n*-hexane, *n*-decane and *n*-hexadecane. *Mol. Phys.*, 100:2471–2475, 2002.

[66] J. P. Nicolas. Molecular dynamics simulation of surfactin molecules at the water-hexane interface. *Biophys. J.*, 85:1377–1391, 2003.

[67] N. Akino, F. Schmid, and M. P. Allen. Molecular-dynamics study of the nematic-isotropic interface. *Phys. Rev. E*, 63:041706, 2001.

[68] Y. Zhang, S. E. Feller, B. R. Brooks, and R. W. Pastor. Computer simulations of liquid/liquid interfaces. I. Theory and application to octane/water. *J. Chem. Phys.*, 103:10252–10266, 1995.

[69] S. Toxvaerd and J. Stecki. Density profiles at a planar liquid-liquid interface. *J. Chem. Phys.*, 102:7163–7168, 1995.

[70] A. R. van Buuren, S. J. Marrink, and H. J. C. Berendsen. A molecular dynamics study of the decane/water interface. *J. Phys. Chem.*, 97:9206–9212, 1993.

[71] D. Michael and I. Benjamin. Solute orientational dynamics and surface roughness of water/hydrocarbon interfaces. *J. Phys. Chem.*, 99:1530–1536, 1995.

[72] D. M. Mitrinović, A. M. Tikhonov, M. Li, Z. Huang, and M. L. Schlossman. Noncapillary wave structure at the water alkane interface. *Phys. Rev. Letters*, 85:582–585, 2000.

[73] A. M. Tikhonov, D. M. Mitrinović, M. Li, Z. Huang, and M. L. Schlossman. An X-ray reflectivity study of the water-docosane interface. *J. Phys. Chem. B*, 104:6336–6339, 2000.

[74] D. M. Mitrinović, Z. Zhang, S. M. Williams, Z. Huang, and M. L. Schlossman. X-ray reflectivity study of the water-hexane interface. *J. Phys. Chem. B*, 103:1779–1782, 1999.

[75] K. Arima, A. Kakinuma, and G. Tamura. Surfactin, a crystalline peptidelipid surfactant produced by *Bacillus subtilis*: isolation, characterization and its inhibition of fibrin clot formation. *Biochem. Biophys. Res. Commun.*, 31:488–494, 1968.

[76] S. Nagai, K. Okimura, N. Kaizawa, K. Ohki, and S. Kanatomo. Study on surfactin, a cyclic depsipeptide. II. Synthesis of surfactin $B_2$ produced by *Bacillus natto* KMD 2311. *Chem. Pharm. Bull.*, 44:5–10, 1996.

[77] Y. Ishigami, M. Osman, H. Nakahara, Y. Sano, R. Ishiguro, and M Matsumoto. Significance of $\beta$-sheet formation for micellization and surface adsorption of surfactin. *Colloids Surf. B Biointerfaces*, 4:341–348, 1995.

[78] F. Peypoux, J. M. Bonmatin, and J. Wallach. Recent trends in the biochemistry of surfactin. *Appl. Microbiol. Biotechnol.*, 51:553–563, 1999.

[79] D. Vollenbroich, G. Pauli, M. Özel, and J. Vater. Antimycoplasma properties and application in cell culture of surfactin, a lipopeptide antibiotic from *Bacillus subtilis*. *Appl. Environ. Microbiol.*, 63:44–49, 1997.

[80] L. Béven and H. Wróblewski. Effect of natural amphipathic peptides on variability, membrane potential, cell shape and motility of mollicutes. *Res. Microbiol.*, 148:163–175, 1997.

[81] M. Kracht, H. Rokos, M. Özel, M. Kowall, G. Pauli, and J. Vater. Antiviral and hemolytic activities of surfactin isoforms and their methyl ester derivatives. *J. Antibiot.*, 52:613–619, 1999.

[82] D. Vollenbroich, M. Özel, J. Vater, R. M. Kamp, and G. Pauli. Mechanism of inactivation of enveloped viruses by biosurfactant surfactin from *Bacillus subtilis*. *Biologicals*, 25:289–297, 1997.

[83] Y. Kameda, S. Ouhira, K. Matsui, S. Kanatomo, T. Hase, and T. Atsusaka. Antitumor activity of *Bacillus natto*. V. Isolation and characterization of surfactin in the culture medium of *Bacillus natto* KMD 2311. *Chem. Pharm. Bull.*, 22:938–944, 1974.

[84] R. Maget-Dana and M. Ptak. Surfactin: interfacial properties and interactions with membrane lipids in mixed monolayers. *Thin Solid Films*, 210:730–732, 1992.

[85] A. Grau, J. C. G. Fernández, F. Peypoux, and A. Ortiz. A study on the interactions of surfactin with lipopeptid vesicles. *Biochim. Biophys. Acta*, 1418:307–319, 1999.

[86] H. Heerklotz and J. Seelig. Detergent-like action of the antibiotic peptide surfactin on lipid membranes. *Biophys. J.*, 81:1547–1554, 2001.

[87] J. M. Bonmatin, M. Genest, H. Labbé, and M. Ptak. Solution three-dimensional structure of surfactin: a cyclic lipopeptide studied by $^1$H-NMR, distance geometry, and molecular dynamics. *Biopolymers*, 34:975–986, 1994.

[88] M. Osman, H. Høiland, H. Holmsen, and Y. Ishigami. Tuning micelles of a bioactive heptapeptide biosurfactant *via* extrinsically induced conformational transition of surfactin assembly. *J. Pept. Sci.*, 4:449–458, 1998.

[89] G. Ferré, F. Besson, and R. Buchet. Conformational studies of the cyclic L,D-lipopeptide surfactin by Fourier transform infrared spectroscopy. *Spectrochim. Acta A Mol. Biomol. Spectrosc.*, 53:623–635, 1997.

[90] E. Vass, F. Besson, Z. Majer, L. Volpon, and M. Hollósi. $Ca^{2+}$-induced changes of surfactin conformation: a FTIR and circular dichroism study. *Biochem. Biophys. Res. Commun.*, 282:361–367, 2001.

[91] H. Razafindralambo, Y. Popineau, M. Deleu, C. Hbid, P. Jacques, P. Thonart, and M. Paquot. Surface-active properties of surfactin/iturin A mixtures produced by *Bacillus subtilis*. *Langmuir*, 13:6026–6031, 1997.

[92] H. Razafindralambo, Y. Popineau, M. Deleu, C. Hbid, P. Jacques, P. Thonart, and M. Paquot. Foaming properties of lipopeptides produced by *Bacillus subtilis*: effect of lipid and peptide structural attributes. *J. Agric. Food Chem.*, 46:911–916, 1998.

[93] X. Gallet, M. Deleu, H. Razafindralambo, P. Jacques, P. Thonart, M. Paquot, and R. Brasseur. Computer simulation of surfactin conformation at a hydrophobic/hydrophilic interface. *Langmuir*, 15:2409–2413, 1999.

[94] J. M. Thornton, M. W. MacArthur, I. K. MacDonald, D. T. Jones, J. B. O. Mitchell, C. L. Nandi, S. L. Price, and M. J. J. M. Zvelebil. Protein structures and complexes: what they reveal about the interactions that stabilize them. *Phil. Trans. R. Soc. Lond. A*, 345:113–129, 1993.

[95] I. K. Mac Donald and J. M. Thornton. Satisfying hydrogen bonding potential in proteins. *J. Mol. Biol.*, 238:777–793, 1994.

[96] A. L. Llamas-Saiz, C. Foces-Foces, O. Mo, M. Yañez, and J. Elguero. Nature of the hydrogen bond: Crystallographic *versus* theoretical description of the O-H$\cdots$N($sp^2$) hydrogen bond. *Acta Crystallogr. B*, 48:700–713, 1992.

[97] P. Debye. *Polar Molecules*. Dover, New York, 1945.

[98] P. E. Smith and W. F. van Gusteren. Translational and rotational diffusion of proteins. *J. Mol. Biol.*, 236:629–636, 1994.

[99] S. Hayward. Peptide-plane flipping in proteins. *Protein Sci.*, 10:2219–2227, 2001.

[100] S. Hovmöller, T. Zhou, and T. Ohlson. Conformations of amino-acids in proteins. *Acta Crystallogr. D Biol. Crystallogr.*, 58:768–776, 2002.

[101] L. Zhong and W. C. Johnson, Jr. Environment affects amino acid preference for secondary structure. *Proc. Natl. Acad. Sci. USA*, 89:4462–4465, 1992.

[102] S. C. Li and C. M. Deber. Peptide environment specifies conformation: helicity of hydrophobic segments compared in aqueous, organic, and membrane environments. *J. Biol. Chem.*, 268:22975–22978, 1993.

[103] C. R. Woese, O. Kandler, and M. L. Wheelis. Towards a natural system of organisms: proposal for the domains Archaea, Bacteria, and Eucarya. *Proc. Natl. Acad. Sci. USA*, 87:4576–4579, 1990.

[104] http://www.tigr.org/.

[105] G. D. Sprott. Structures of archaebacterial membrane lipids. *J. Bioenerg. Biomembr.*, 24:555–566, 1992.

[106] M. M. Jr. Kenneth and B. Roux. *Biological membranes: a molecular perspective from computation and experiment*. Birkhäuser, Boston, 1996.

[107] J. L. C. M. van de Vossenberg, A. J. M. Driessen, and W. N. Konings. The essence of being extremophilic: the role of the unique archaeal membrane lipids. *Extremophiles*, 2:163–170, 1998.

[108] G. Darlant, T. D. Brock, W. Samsonoff, and S. F. Conti. A thermophilic, acidophilic mycoplasma isolated from a coal refuse pile. *Science*, 170:1416–1418, 1970.

[109] M. Swain, J. R. Brisson, G. D. Sprott, F. P. Cooper, and G. B. Patel. Identification of $\beta$-L-gulose as the sugar moiety of the main polar lipid *Thermoplasma acidophilum*. *Biochim. Biophys. Acta*, 1345:56–64, 1997.

[110] J. L. Gabriel and P. L. G. Chong. Molecular modeling of archaebacterial bipolar tetraether lipid membranes. *Chem. Phys. Lipids*, 105:193–200, 2000.

[111] M. de Rosa, A. Gambacorta, and B. Nicolaus. A new type of cell membrane, in thermophilic archaebacteria, based on bipolar ether lipids. *J. Membr. Sci.*, 16:287–294, 1983.

[112] A. Gliozzi, M. Robello, A. Relini, and G. Accardo. Asymmetric black membranes formed by one monolayer of bipolar lipids at the air/water interface. *Biochim. Biophys. Acta*, 1189:96–100, 1994.

[113] O. Lockhoff and P. Stadler. Syntheses of glycosylamides as glycolipid analogs. *Carbohydr. Res.*, 314:13–24, 1998.

[114] G. Lecollinet, R. Auzély-Velty, T. Benvegnu, G. Mackenzie, J. W. Goodby, and D. Plusquellec. An efficient synthesis of analogues of unsymmetrical archaeal tetraether glycolipids. *Chem. Comm.*, 15:1571–1572, 1998.

[115] G. Lecollinet, R. Auzély-Velty, M. Danel, T. Benvegnu, G. Mackenzie, J. W. Goodby, and D. Plusquellec. Synthetic approaches to novel archaeal tetraether glycolipid analogues. *J. Org. Chem.*, 64:3139–3150, 1999.

[116] G. Lecollinet, A. Gulik, G. Mackenzie, J. W. Goodby, T. Benvegnu, and D. Plusquellec. Supramolecular self-assembling properties of membrane-spanning archaeal tetraether glycolipid analogues. *Chem. Eur. J.*, 8:585–593, 2002.

[117] T. Benvegnu, G. Lecollinet, J. Guilbot, M. Roussel, M. Brard, and D. Plusquellec. Novel bolaamphiphiles with saccharidic polar headgroups: synthesis and supramolecular self-assemblies. *Polym. Int.*, 52:500–506, 2003.

[118] I. Uda, A. Sugai, K. Kon, S. Ando, Y. H. Itoh, and T. Itoh. Isolation and characterization of novel neutral glycolipids from *Thermoplasma acidophilum*. *Biochim. Biophys. Acta*, 1439:363–370, 1999.

[119] I. Uda, A. Sugai, A. Shimizu, Y. H. Itoh, and T. Itoh. Glucosylcaldarchaetidylglycerol, a minor phosphoglycolipid from *Thermoplasma acidophilum*. *Biochim. Biophys. Acta*, 1484:83–86, 2000.

[120] S. G. Batrakov, T. A. Pivovarova, S. E. Esipov, V. I. Sheichenko, and G. I. Karavaiko. $\beta$-D-Glucopyranosyl caldarchaetidylglycerol is the main lipid of the acidophilic, mesophilic, ferrous iron-oxidising archaeon *Ferroplasma acidiphilum*. *Biochim. Biophys. Acta*, 1581:29–35, 2002.

[121] J. W. Goodby, G. H. Mehl, I. M. Saez, R. P. Tuffin, G. Mackenzie, R. Auzély-Velty, T. Benvegnu, and D. Plusquellec. Liquid crystals with restricted molecu-

lar topologies: supermolecules and supramolecular assemblies. *Chem. Comm.*, 19:2057–2069, 1998.

[122] T. Baba, Y. Toshima, H. Minamikawa, M. Hato, K. Suzuki, and N. Kamo. Formation and characterization of planar lipid bilayer membranes from synthetic phytanyl-chained glycerolipids. *Biochim. Biophys. Acta*, 1421:91–102, 1999.

[123] O. Dannenmuller, K. Arakawa, T. Eguchi, K. Kakinuma, S. Blanc, A. M. Albrecht, M. Schmutz, Y. Nakatani, and G. Ourisson. Membrane properties of archaeal macrocyclic diether phospholipids. *Chem. Eur. J.*, 6:645–654, 2000.

[124] S. M. Bezrukov. Functional consequences of lipid packing stress. *Curr. Opin. Colloid Interf. Sci.*, 5:237–243, 2000.

[125] U. Bakowsky, U. Rothe, E. Antonopoulos, T. Martini, L. Henkel, and H. J. Freisleben. Monomolecular organization of the main tetraether lipid from *Thermoplasma acidophilum* at the water-air interface. *Chem. Phys. Lipids*, 105:31–42, 2000.

[126] S. V. Albers, J. L. C. M. van de Vossenberg, A. J. M. Driessen, and W. N. Konings. Adaptations of the archaeal cell membrane to heat stress. *Front. Biosci.*, 5:813–820, 2000.

[127] J. C. Mathai, G. D. Sprott, and M. L. Zeidel. Molecular mechanisms of water and solute transport across archaebacterial lipid membranes. *J. Biol. Chem.*, 276:27266–27271, 2001.

[128] M. J. Hanford and T. L. Peeples. Archaeal tetraether lipids: unique structures and applications. *Applied Biochem. Biotech.*, 97:45–62, 2002.

[129] A. Gliozzi, A. Relini, and P. L. G. Chong. Structure and permeability properties of biomimetic membranes of bolaform archaeal tetraether lipids. *J. Membr. Sci.*, 206:131–147, 2002.

[130] C. Strobl, L. Six, K. Heckmann, B. Henkel, and K. Ring. Physicochemical characterization of tetraether lipids from *Thermoplasma acidophilum* II. Film balance studies on the monomolecular organization of the main glycophospholipid in monofilms. *Z. Naturforsch.*, 40c:219–222, 1985.

[131] H. C. Jarrell, K. A. Zukotynski, and G. D. Sprott. Lateral diffusion of the total polar lipids from *Thermoplasma acidophilum* in multilamellar liposomes. *Biochim. Biophys. Acta*, 1369:259–266, 1998.

# Summary

The aim of this work is to study, by computer simulations, various interfaces and their properties. We have used different interface models: a simple two phases system (liquid-vapour alkane, an oil-like molecule), a hydrophobic-hydrophilic interface (liquid-liquid water-hexane, an alkane), a similar interface containing a surfactant lipopeptide (surfactin), and a biological membrane made of spanning lipids from archaebacteria. This work has been done using the molecular dynamics technique (MD), and almost all the models have been described at an atomic scale, providing a realistic representation of the modelled materials.

First, we introduce in chapter 1 the terms used in this work, define the scope of the thesis, and give a very brief description of the molecular dynamics (MD) technique.

The first part (A) of the manuscript reports both the study of a liquid-vapour alkane model (chapter 2) and the study of a hexane-water liquid-liquid interface (chapter 3). We present in the former chapter a method of interfacial tension calculation, and probe it for a range of linear alkane lengths, two ranges of temperature, and two sets of force field parameters (set of parameters which give a representation of the molecular properties and dynamics). The implementation of the method used gives interfacial tension predictions in nice agreement with experiments. In the latter chapter, we study the topology and properties of the interface. The interfacial broadening from capillary waves (small waves occuring at the interface and responsible for an 'interfacial width') is, for the first time, investigated both qualitatively and quantitatively, for a non-ideal liquid-liquid system. We found that the interfacial widths calculated from computer simulations are much smaller than the widths predicted from the capillary waves theory. We suggest that the apparent disagreement comes from the correlation length parameter (defined as the minimum length between two particles with uncorrelated motions) often taken as a molecular length or diameter in the litterature.

The second part (B, chapter 4) of the manuscript concerns the study of a bio-surfactant (surfactin, a lipopeptide composed of seven amino-acid residues and a long aliphatic chain, which is oil-like) at the water-hexane interface. This molecule is an efficient surfactant, decreasing the water surface tension by a factor 2 at low concentration. Moreover, experimental results suggest that this molecule exhibits various interesting biological properties. This is the first extensive and realistic MD simulation of surfactin done at a hydrophobic-hydrophilic interface. We have investigated the molecular motions, the peptide folding, the intra- and inter- molecular hydrogen bonds, and the dynamics of the surfactin. This surfactant exhibits a 'chimeric' geometry depending on the interfacial concentration of surfactants. The molecule has a stable structure and is tensioactive at a sufficient interfacial concentration. Below this limit, the molecule is in a 'horse-saddle' shape, but none of the hydrogen bonds is conserved, and the dihedral angles characteristic for the amino-acid residues (Ramachandran angles) fluctuate a lot.

The last part (C, chapter 5) presents the first long MD study of five tetraether lipid membrane models. The models differ with respect to the number of cyclopentane rings per lipid molecule, and their positions. Cyclopentane rings are supposed to maintain the low permeability of the membrane at high temperatures. We have investigated their effects on the membrane properties by the study of the five different models. Furthermore, the absolute configuration of the the carbons linking the rings to the rest of the chain differs from one side of the chain to the other one (which means they are chiral, thus, as two hands, cannot be superimosed). We investigate the membrane physical properties and the membrane organization. We report the dependence of the lipid membrane topology on the lipid structure, and more specifically the presence of rings on the aliphatic chains. Moreover, we correlate the pressure profile to the absolute configuration of the aliphatic carbons, by the comparison between the pressure profiles of each hydrophobic side of the membrane.

# Samenvatting (Summary in Dutch)

Dit proefschrift gaat over grensvlakken. In de drie delen waaruit het proefschrift is opgebouwd worden met behulp van computersimulaties grensvlaksystemen van toenemende complexiteit bestudeerd. Dit begint met een relatief eenvoudig tweefasensysteem gevormd door de vloeibare- en dampfase van alkanen en het grensvlak tussen twee niet mengbare vloeistoffen, in dit geval water en hexaan. In het tweede deel wordt gekeken naar de invloed van het bio-surfactant surfactin op de eigenschappen van de water-hexaan grenslaag. Het derde deel tenslotte, is gewijd aan een grenslaag tussen binnen- en buitenwereld gevormd door een biologisch membraan. Vrijwel alle modellen zijn met moleculaire dynamica (MD) op atomaire schaal berekend, wat een realistische representatie van de gemodelleerde systemen oplevert.

Voordat tot het eigenlijke onderwerp van dit proefschrift wordt overgegaan is het goed een overzicht te hebben van de gebruikte terminologie en de achtergrond en reikwijdte van het werk. In een inleidend hoofdstuk (1) zullen deze onderwerpen kort aan de orde komen, tesamen met een korte beschrijving van de gebruikte moleculaire dynamica techniek.

Zoals gezegd, wordt in het eerste deel aandacht besteed aan het grensvlak tussen vloeistof en damp van alkanen. In hoofdstuk 2 wordt een tweetal modellen voor de beschrijving van interacties tussen alkanen met elkaar vergeleken om inzicht te krijgen in de relatie tussen de details van de moleculaire interacties en de berekende oppervlaktespanning. Vergelijking van de berekeningen voor verschillende lineaire alkanen en voor verschillende temperatuurgebieden met experimenteel verkregen data leidt tot een model waarbij de berekende oppervlaktespanning van alkanen in goede overeenstemming is met de experimenteel verkregen resultaten. In hoofdstuk 3 wordt een studie van de topologie en eigenschappen van het grensvlak tussen water en hexaan beschreven. De resultaten van moleculaire dynamica berekeningen worden

vergeleken met die van de capillaire golftheorie. Het blijkt dat de dikte van de grenslaag verkregen met de moleculaire dynamica berekeningen aanzienlijk kleiner is dan de dikte die via de capillaire golftheorie wordt berekend. Door een herziening van de definitie van de zogenaamde correlatielengteparameter die een maat is voor de afstand waarop moleculaire bewegingen nog aan elkaar gerelateerd zijn, zijn de resultaten goed met elkaar in overeenstemming te brengen.

In het tweede deel (hoofdstuk 4) richt de aandacht zich op het biologisch molecule met oppervlakte actieve eigenschappen, surfactin. Het door bacteriën geproduceerde molecule blijkt behalve oppervlakte actief te zijn ook een aantal andere interessante biologische eigenschappen te bezitten, waaronder antibacteriele en antivirale activiteit. Het molecule bestaat uit een waterafstotende vetzuur staart en een "kopgroep" bestaande uit zeven aminozuren. Het hier gepresenteerde werk is de eerste realistische MD simulatie van surfactin aan een hydrofiel-hydrofoob grensvlak. Gekeken wordt hoe dynamica, structuur en interacties met de omgeving van surfactin veranderen afhankelijk van de concentratie van surfactin aan het grensvlak. Het blijkt dat bij lage concentraties de vorm van het molecule vergelijkbaar is met een zadelvorm. Bij voldoende hoge concentratie aan het grensvlak clusteren de moleculen waardoor de interacties van de hydrofobe delen met het hydrofiele medium geminimaliseerd worden. Deze clusters worden voornamelijk gestabiliseerd door van der Waals interacties.

Het onderwerp van het laatste deel zijn biologische membranen, zoals deze worden aangetroffen in archaebacteriën. Er wordt een vijftal modelmembranen bestudeerd die bestaan uit tetra-etherlipiden. De modellen verschillen in het aantal en de positie van cyclopentaanringen per lipidemolecule. De cyclopentaan ringen worden verondersteld een rol te spelen bij het in stand houden van een lage membraanpermeabiliteit bij hoge temperaturen. De fysische eigenschappen en de structuur van de membranen voor de verschillende membraanmodellen werd onderzocht waarbij vooral gekeken werd naar de afhankelijkheid van de positie en de chiraliteit van de cyclopentaanringen. Een van de resultaten is dat een duidelijke correlatie gevonden wordt tussen de conformatie van de alifatische koolstofatomen en het drukprofiel van het membraan.

# Publications

- F. Charbonnier, J.P. Nicolas, L. Eveleigh, P. Hapiot, J. Pinson, and C. Rolando, "Chemistry in electrospray mist: red-ox reactivity of nitro-halogenated aromatics during negative ion production", *Comp. R. Ac. Sci. IIc*, 1998, 1(7), 449-456.
- J.P. Nicolas and B. Smit, "Molecular dynamics simulations of the surface tension of $n$-hexane, $n$-decane and $n$-hexadecane", *Mol. Phys.*, 2002, 100(15), 2471-2475.
- J.P. Nicolas and N.R. de Souza, "Molecular dynamics study of $n$-hexane–water interface: towards a better understanding of the liquid-liquid interfacial broadening", *J. Chem. Phys.*, in press.
- N.R. de Souza and J.P. Nicolas, "Molecular dynamics study of the alkane liquid-vapor interfacial broadening", in preparation.
- J.P. Nicolas, "Molecular dynamics simulation of surfactin at the hexane-water interface", *Biophys. J.*, 2003, 85, 1377-1391.
- J.P. Nicolas, "Molecular dynamics study of surfactin folding-unfolding at a hydrophobic-hydrophilic interface", in preparation.
- J.P. Nicolas and B. Smit, "Molecular dynamics simulation of hydrated tetraether lipid membranes at low temperature", in preparation.
- M. Kranenburg, J.P. Nicolas, and B. Smit, "The coarsegraining of a phospholipid", in preparation.

# Acknowledgments


- I thank my promotor Berend Smit, who invited me a few years ago to start a PhD in his group. During my thesis, he gave me more freedom in my work that one could ever hope for. I will miss it.

- I thank people with whom I have collaborated with, Berend, Nicolas de Souza and Marieke Kranenburg, and people who have supported me, Thijs Vlugt, Maddalena Venturoli, Gooitzen Zwanenburg, Jochem Wichers-Hoeth, Marijke Duyvendak, Jan Geenevasen, Klaas Hellingwerf, Mickaëlle Brard, and Thierry Benvegnu.

- I thank people who have contributed to "customize" my work contract when my son needed my presence, and by extention, people who took care of him until he came to Holland. At the University, this has involved many people I am indebted to, from Berend to Karen Tensen.

- I will never forget the warm atmosphere from the ITS team and its members as Nicolas, Elio, Maddalena, Thijs, Simona, Daniele, Titus, Gooitzen, and visitors as Carine.

- I thank people who took care of me in Amsterdam, Jannie and Steef, Gery, the Mazereeuw family, and Santi and Nicolas.

- I thank Corinne, Thomas, our family, and our friends, for their moral support during this thesis.